https://doi.org/10.5194/wcd-2019-8
Preprint. Discussion started: 1 October 2019

Weather and Climate Dynamics Discussions
Open Access
EGU

Idealised simulations of cyclones with robust symmetrically-unstable sting jets

Ambrogio Volonté[1,2], Peter A. Clark[1], and Suzanne L. Gray[1]

[1]Department of Meteorology, University of Reading, Reading, RG6 6BB, UK
[2]National Centre for Atmospheric Science-Climate, University of Reading, Reading, RG6 6BB, UK

Correspondence: Ambrogio Volonté (a.volonte@reading.ac.uk)

Abstract. Idealised simulations of Shapiro-Keyser cyclones developing a sting jet (SJ) are presented. Thanks to an improved and accurate implementation of thermal wind balance in the initial state, it has been possible to use more realistic environments than in previous idealised studies. As a consequence, this study provides further insight in SJ evolution and dynamics and explores SJ robustness to different environmental conditions, assessed via a wide and different range of sensitivity experiments.

The control simulation contains a cyclone that fits the Shapiro-Keyser conceptual model and develops a SJ whose dynamics are associated with the evolution of mesoscale instabilities including symmetric instability (SI) along the airstream. The SJ undergoes a strong descent while leaving the cloud-head banded tip and markedly accelerating towards the frontal-fracture region, revealed as an area of buckling of the already-sloped moist isentropes. A substantial amount of SI, generated by slantwise frontal motions in the cloud head, is released along the SJ during its descent. This supports the role of SI in the airstream's dynamics proposed in a conceptual model outlined in a previous study.

Sensitivity experiments illustrate that the SJ is a robust feature of intense Shapiro-Keyser cyclones, highlighting a range of different environmental conditions in which SI contributes to the evolution of this airstream, conditional on the model having adequate resolution. The results reveal that several environmental factors can modulate the strength of the SJ. However, a positive relationship between the strength of the SJ, both in terms of peak speed and amount of descent, and the amount of instability occurring along it can still be identified.

In summary, the idealised simulations presented in this study show the robustness of SJ occurrence in intense Shapiro-Keyser cyclones and support and clarify the role of dry instabilities in SJ dynamics.

1 Introduction

The current state of knowledge about sting jets (SJs) was recently reviewed by Clark and Gray (2018) (CG18 hereafter). SJs are coherent air streams in extratropical cyclones that descend from mid-levels within the cloud head and accelerate into a frontal-fracture region. Frontal fracture is characteristic of cyclones that evolve according to the Shapiro-Keyser conceptual model (Shapiro and Keyser, 1990). SJs descend towards the top of the boundary layer (lying above the cold conveyor belt jet for at least part of the cyclone lifecycle) and can lead to localised transient strong, damaging, winds if their associated strong momentum is mixed down to the ground. The SJ is distinct in location, lifespan and spatial scale from the synoptic-scale cold

https://doi.org/10.5194/wcd-2019-8
Preprint. Discussion started: 1 October 2019

and warm conveyor belts that exist in most cyclones. However, it is difficult to distinguish the SJ from the cold conveyor belt using surface observations alone. As a result, there are relatively few in-depth studies of SJs in observed cyclones, and certainly not enough to allow more than qualitative conclusions regarding the relationship between SJ structure and precursor characteristics. Here we use idealised simulations of SJ-containing cyclones developing in a realistic atmospheric environment to explore the robustness of SJ generation and characteristics for a wide range of environmental background states and assess the importance of dry mesoscale instability release in the generation of the SJ.

Climatological analyses using the existence of atmospheric instability in the cloud head as a predictor of likelihood that a cyclone will produce a SJ have revealed that SJs are probably a common feature of cyclones: Hart et al. (2017) found 32% of all extended winter North Atlantic cyclones had the required instability, increasing to 42% in the 22% of those cyclones that developed explosively. The proportion of cyclones with SJs may also increase in a future warmer climate (Martínez-Alvarado et al., 2018). Although the proportion of cyclones with SJs that lead to strong surface winds is not known, the likely current and future prevalence of cyclones with SJs and diagnosed presence of SJs in case studies of damaging European cyclones such as the Great October storm (Browning, 2004) and the St. Jude's day storm (Browning et al., 2015) motivates further research into their characteristics.

In the time since SJs were first formally identified in Browning (2004) detailed case studies of about ten SJ-containing cyclones have been published (see list in Table 2 in CG18). These analyses have revealed many common features and led to the development of the commonly-accepted definition given above. More contentious has been attribution of SJs to a mechanism with large-scale dynamics, the release of mesoscale instabilities (conditional symmetric instability (CSI), symmetric instability (SI), inertial instability (II) and conditional instability (CI)), evaporative cooling and frontal dynamics all evidenced as being associated with SJ descent (see section 5 of CG18). Consequently, it is concluded in that review that it is likely that a continuum of behaviour occurs with release of mesoscale instability (if it occurs) enhancing the SJ strength beyond that which can be achieved through frontal dynamics in the frontolytic region at the tip of the cloud head. In contrast to most previous studies, here we focus on the importance of dry, rather than moist, mesoscale instabilities for SJ enhancement.

Although mesoscale instability presence and release has been diagnosed in many case studies (e.g. the study of windstorm Friedhelm by Martínez-Alvarado et al. (2014)), the control of the atmospheric environment afforded by moist idealised simulations of SJ cyclones makes them an ideal tool for exploring the range of instabilities that may occur and their impact on SJ characteristics. Baker et al. (2014) produced the first analysis of idealised simulations of SJs in cyclones and found that, while the presence of a SJ was robust to the environmental state in which the cyclone developed, the existence of the different mesoscale instabilities varied with CSI release occurring along the SJ in the control simulation and II and CI release occurring in the simulation with the weakest static stability. In their idealised simulations Coronel et al. (2016) found spatially-localised regions of negative saturated equivalent moist potential vorticity (MPV*, for which negative values imply the presence of mesoscale instability) and near-zero MPV* values along diagnosed SJ trajectories. The authors interpreted this finding as implying that the environment was near-neutral to CSI. However, as explained in CG18, another interpretation is that the near-neutral condition is evidence of CSI having been (or continuously being) released. Buckled absolute momentum surfaces were also generated in the Coronel et al. (2016) study implying that II existed.

https://doi.org/10.5194/wcd-2019-8
Preprint. Discussion started: 1 October 2019

While both these idealised modelling studies produced cyclones with characteristics consistent with those of observed SJ cyclones, the atmospheric environments were cooler (and in Coronel et al. (2016) also drier) than typically observed, likely due to the constraints involved in designing idealised environments: Baker et al. (2014) used a near -freezing surface temperature, though their initial relative humidity was 80%, and Coronel et al. (2016) also used cool temperatures together with a lower-tropospheric relative humidity of 60%. In this study we have overcome these constraints and have used environments that are more consistent with those observed. We also explore a different range of parameter values and parameters to these previous studies. Baker et al. (2014) only presented results of changing the initial tropospheric static stability of the environmental state in their moist simulation in their paper (as changing this parameter was found to have the greatest effect on the strength and descent rate of the resulting sting jet), although the dependence on upper-tropospheric jet strength, stratospheric static stability and cyclonic barotropic shear were also explored by the authors and the results of these experiments are presented in the associated PhD thesis (Baker, 2011). Coronel et al. (2016) explored the sensitivity of the SJ cyclone and SJ to whether or not it is initialised to the warm south side, or on, the upper-tropospheric zonal jet axis and also to model resolution (considering three resolution configurations from the four possible with horizontal grid spacings of 20 km and 4 km and two different vertical resolutions). In our study we explore the sensitivity of SJs to horizontal resolution, initial state relative humidity, upper-tropospheric jet strength, and surface temperature.

Our focus on the importance of dry mesoscale instabilities for SJ generation is motivated by our recent analysis of windstorm Tini (Volonté et al., 2018). In that study we demonstrated that mesoscale instability release occurring in a higher-resolution simulation enhanced the strong winds in the frontal-fracture region occurring through synoptic-scale cyclone dynamics (from comparison with results from a coarser-resolution simulation that was not able to represent mesoscale instability release). We also found that the SJ first became largely unstable to CSI and then to SI and II. Most previous moist studies that have assessed the role of mesoscale instability release in SJ generation have not explicitly considered SI though some have considered II e.g. Martínez-Alvarado et al. (2014) and Baker et al. (2014) both considered CSI, CI, and II. As noted in CG18, as the environment in an intense extratropical cyclone is unlikely to the strictly barotropic, a diagnosis of II should probably be interpreted as implying the presence of SI. However, in Volonté et al. (2018) we distinguished between II diagnosed through negative values of the vertical component absolute vorticity, ζ_z, and SI diagnosed through negative potential vorticity (PV). Finally, we proposed that the generation of negative MPV*, and later negative PV, occurs through the tilting of horizontal ζ generated by frontal ascent and descent in the cloud head to produce negative values of the vertical component of ζ which is then amplified prior to the final stage pf descent of the SJ by stretching. We further explore this proposed mechanism in the current study.

The structure of this paper is as follows. The methods are described in Sec. 2 starting with the idealised model configuration and setup of the initial environmental state (Sec. 2.1) and followed by the diagnostics used for mesoscale instability (Sec. 2.2), the trajectory method (Sec. 2.3) and the rationale for the sensitivity experiments (Sec. 2.4). The results section (Sec. 3) starts with an analysis of the SJ in the cyclone in the control simulation (Sec. 3.1) and is followed by analysis of the dependence of the SJ on the environmental initial state through the sensitivity experiments (Sec. 3.2). Section 4 contains a discussion of these results and the overall conclusions.

2 Data and Methodology

2.1 Model configuration and chosen initial state

2.1.1 Background

The initial base state used is inspired by Polvani and Esler (2007), referred to as PE hereafter. In this study an improved estimation of balanced base state and a method to adjust the entire vertical virtual potential temperature (θ_v) profile to make that at the jet centre equal to the reference has been devised, the details of which are given in the next section. As a result of this improvement, the instability issues described in Baker et al. (2014) are no longer present and so it has been possible to use a more realistic temperature profile with a central value of potential temperature of 295 K at the surface, as opposed to the rather cold temperatures occurring in the former study. The SJ occurring in the control simulation has values of wet bulb potential temperature (θ_w) around 285 K, ∼10 K warmer than the ones in the idealised simulation of Baker et al. (2014) and the high horizontal and vertical resolution idealised simulation of Coronel et al. (2016) (which were about 276 K and 274 K (for the warmest trajectory), respectively). The SJ analysed in a simulation of the Great Storm (Clark et al., 2005) had θ_w around 286 K while simulations of Gudrun (Baker, 2011), Ulli (Smart and Browning, 2014) and Tini (Volonté et al., 2018) produced SJs with θ_w around 279 K, 281 K and 278 K, respectively. Hence, the thermal properties of the SJs generated in the idealised simulations presented in this paper are consistent with those analysed in case studies, particularly warm ones like in the Great Storm.

The simulations described in this paper are performed in a spherical geometry, with the periodic channel extending from 12°N to 78.5°N in latitude and from 20°W to 25°E in longitude. The initial state is designed to develop an LC1-type cyclone. Thorncroft et al. (1993) highlighted that LC1 cyclones develop similarly to the Shapiro-Keyser conceptual model with the occurrence of frontal fracture and, in later stages, a warm seclusion.

2.1.2 Model Configuration

The MetUM is a finite difference model that solves the non-hydrostatic deep atmosphere dynamical equations on a sphere (White et al., 2005). The equations of motion are based on those of the 'New Dynamics' (Davies et al., 2005), as used by Baker et al. (2014):

$$\frac{\mathrm{D}u}{\mathrm{D}t} = \frac{uv\tan\phi}{r} - \frac{uw}{r} + f_3 v - f_2 w - \frac{c_{pd}\theta_v}{r\cos\phi}\left(\frac{\partial\Pi}{\partial\lambda} - \frac{\partial\Pi}{\partial r}\frac{\partial r}{\partial\lambda}\right) + S^u, \tag{1}$$

$$\frac{\mathrm{D}v}{\mathrm{D}t} = \frac{u^2\tan\phi}{r} - \frac{vw}{r} + f_1 w - f_3 u - \frac{c_{pd}\theta_v}{r}\left(\frac{\partial\Pi}{\partial\phi} - \frac{\partial\Pi}{\partial r}\frac{\partial r}{\partial\phi}\right) + S^v, \tag{2}$$

$$\frac{\mathrm{D}w}{\mathrm{D}t} = \frac{u^2+v^2}{r} + f_2 u - f_1 v - g - c_{pd}\theta_v\frac{\partial\Pi}{\partial r} + S^w, \tag{3}$$

https://doi.org/10.5194/wcd-2019-8
Preprint. Discussion started: 1 October 2019

where:

$$\frac{\mathrm{D}}{\mathrm{D}t} \equiv \frac{\partial}{\partial t} + \frac{u}{r\cos\phi}\frac{\partial}{\partial \lambda} + \frac{v}{r}\frac{\partial}{\partial \phi} + \dot{\eta}\frac{\partial}{\partial \eta}, \tag{4}$$

$$\Pi = \left(\frac{p}{p_0}\right)^{\frac{R_d}{c_{pd}}}; \quad p_0 = 10^5 \text{ Pa}, \tag{5}$$

and

$$\theta_v = \frac{T}{\Pi}\left(\frac{1+\frac{1}{\epsilon}m_v}{1+m_v+m_{cl}+m_{cf}}\right); \quad \epsilon = \frac{R_d}{R_v} = 0.622. \tag{6}$$

Here, (u,v,w) are the three components of vector wind, p the pressure, T the temperature, m_v, m_{cl} and m_{cf} mixing ratios of vapour, liquid water and ice cloud respectively and c_{pd} is the specific heat capacity of dry air at constant pressure. S^{χ} represents a source term in χ. Time is denoted t. The spherical polar spatial coordinates are (λ,ϕ,r), while η is a generalised vertical coordinate. All derivatives with respect to λ and ϕ (i.e. 'horizontal' derivatives) are along constant η surfaces. The Coriolis terms are given by

$$(f_1, f_2, f_3) = 2\Omega\,(0, \cos\phi, \sin\phi) \tag{7}$$

on an unrotated grid.

The new dynamical core introduced operationally in 2014, ENDGAME, solves the same equations (with more accurate numerical methods) but does not use θ or θ_v as prognostic — all variables are related to *dry* density, ρ_d (i.e. the density of the air not including water vapour), so

$$\rho = \rho_d\left(1+\sum m_X\right) = \rho_d\,(1+m_v)\,, \tag{8}$$

where $\sum m_X$ is the sum of all water species and this reduces to m_v in our case. Similarly,

$$\theta_{vd} = \theta\left(1+\frac{1}{\epsilon}m_v\right) \tag{9}$$

and

$$\theta_v = \frac{\theta_{vd}}{(1+\sum m_X)}. \tag{10}$$

The equation of state is thus

$$\rho_d = \left(\frac{p_0}{R_d}\right)\frac{\Pi^{\frac{1-\kappa_d}{\kappa_d}}}{\theta_{vd}} \tag{11}$$

Alternative forms include:

$$p = R_d\rho_d T_{vd} = R_d \rho T_v. \tag{12}$$

https://doi.org/10.5194/wcd-2019-8
Preprint. Discussion started: 1 October 2019

The integration scheme is semi-implicit and semi-Lagrangian (Wood et al., 2014) (though the inherently conservative version was not used as it is very computationally expensive). The model uses Arakawa C staggering in the horizontal (Arakawa and Lamb, 1977) and a terrain-following hybrid-height Charney-Phillips vertical coordinate (Charney and Phillips, 1953). Model parametrizations include longwave and shortwave radiation (Edwards and Slingo, 1996), boundary-layer mixing (Lock et al., 2000), sub-grid cloud condensation (Smith, 1990), cloud microphysics and large-scale precipitation (Wilson and Ballard, 1999) and convection (Gregory and Rowntree, 1990). The initial state described below was implemented in Version 10.5 of the MetUM.

2.1.3 Thermal wind balance for uniform zonal flow

Since MetUM solves non-hydrostatic deep atmosphere equations on a sphere, traditional derivations of thermal wind balance need some modification. Previous studies using the MetUM (Boutle et al., 2011; Baker et al., 2014) used an approximate solution based on hydrostatic balance in a shallow atmosphere and introduced a 'balancing step' to allow the model to adjust to a true balance. However, we have derived a more accurate initial state which avoids this requirement. For balanced zonal flow $v = w = 0$, $u \equiv u(\phi, \eta)$. With no surface orography $r \equiv r(\eta)$. Then, ignoring source terms, eqs. (1) to (3) become, after some rearrangement:

$$\frac{\partial \Pi}{\partial \lambda} = 0 \tag{13}$$

$$c_{pd}\frac{\partial \Pi}{\partial \phi} = \frac{A}{\theta_v}; \quad A = u^2 \tan\phi - f_3 u r \tag{14}$$

$$c_{pd}\frac{\partial \Pi}{\partial r} = \frac{B}{\theta_v}; \quad B = \frac{u^2}{r} + f_2 u - g \tag{15}$$

The last of these expresses quasi-hydrostatic balance (White et al., 2005).

The next step is to eliminate the Exner pressure by differentiating eq. (14) with respect to r and eq. (15) with respect to ϕ to obtain the thermal wind relationship:

$$\frac{1}{\theta_v}\frac{\partial A}{\partial r} - \frac{A}{\theta_v^2}\frac{\partial \theta_v}{\partial r} = \frac{1}{\theta_v}\frac{\partial B}{\partial \phi} - \frac{B}{\theta_v^2}\frac{\partial \theta_v}{\partial \phi} \tag{16}$$

Thus:

$$B\frac{\partial \ln\theta_v}{\partial \phi} = \frac{\partial B}{\partial \phi} + A\frac{\partial \ln\theta_v}{\partial r} - \frac{\partial A}{\partial r} \tag{17}$$

In Hydrostatic Primitive Equations, $A \equiv -f_3 u r$, $B \equiv -g$, and the second term on the right hand side can be neglected.

Starting from a reference profile, $\theta_v^{ref}(r)$, we can formally integrate thus:

$$\theta_v(r,\phi) = \theta_v^{ref}(r)\,\frac{B(r,\phi)}{B(r,\phi_s)}\exp\left(-\int_{\phi_s}^{\phi}\frac{1}{B}\left[\frac{\partial A}{\partial r} - A\frac{\partial \ln\theta_v}{\partial r}\right]\mathrm{d}\phi'\right). \tag{18}$$

https://doi.org/10.5194/wcd-2019-8
Preprint. Discussion started: 1 October 2019

This is an implicit equation for θ_v if we specify u. The first term in the integral is related to the thermal wind. The second is related to the stability. We anticipate that the thermal wind will only have a small impact on the stability so using θ_v^{ref} in this term is probably a good approximation. This suggests an iterative approach, using this as a starting estimate, then refining the estimate using the previous iteration in this term. In practice this iteration has proven unnecessary; using θ_v^{ref} leads to a well-balanced state and our final (approximate) solution is:

$$\theta_v(r,\phi) = \theta_v^{ref}(r)\frac{B(r,\phi)}{B(r,\phi_s)}\exp\left(-\int_{\phi_s}^{\phi}\frac{1}{B}\left[\frac{\partial A}{\partial r} - A\frac{\partial \ln\theta_v^{ref}}{\partial r}\right]\mathrm{d}\phi'\right). \tag{19}$$

PE point out that the LC1 setup has zero wind at the surface, so it is sufficient to set the surface pressure to $p_s = 1000$ hPa. They use pressure coordinates and so integrate the hydrostatic balance equation to obtain the height of pressure levels. The equivalent in height coordinates is, from eq. (15):

$$\Pi(r) = \Pi_s + \int_0^r \frac{B}{c_{pd}\theta_v}\mathrm{d}r, \tag{20}$$

where $\Pi_s = (p_s/p_0)^{R_d/c_{pd}}$, most conveniently set to 1 for the LC1 setup. This gives us a slight problem, in that Π is stored on model ρ levels. If we assume an adiabatic layer at the surface, then we can compute Π at the first ρ level and continue from there upwards.

More generally, there is a non-zero zonal wind at the surface. PE address this through an iterative procedure, as they are working in pressure coordinates which do not coincide with the surface. However, we have taken a non-iterative approach based upon that used by Boutle et al. (2011) and Baker et al. (2014) and improved in the balance adjustment.

Their algorithm, that we shall call 'profile correction option 1', makes a correction to the temperature that is as follows: the vertical θ_v profile is adjusted everywhere using a constant value to make that at the surface at the jet centre equal to the reference. If we call the result of eq. (19) θ_v^1 then

$$\theta_v(r,\phi) = \theta_v^1(r,\phi) - \theta_v^1(a,\phi_0) + \theta_v^{ref}(a) \tag{21}$$

where ϕ_0 is the jet centre and a is the value of r at the surface.

The algorithm used in this study, that we shall call 'profile correction option 2', seeks instead to adjust the entire vertical θ_v profile everywhere to make that at the jet centre equal to the reference. Thus an adjustment is made which is a function of r only. The factor multiplying θ_v^{ref} in eq. (19) is just a function of u, and hence r and ϕ, say $H(r,\phi)$. Using θ_v^{ref} in the integral on the right hand side we can write:

$$\theta_v(r,\phi) = \left(\theta_v^{ref}(r) + \theta_{corr}(r)\right)H(r,\phi). \tag{22}$$

We define θ_v^1 as the solution with $\theta_{corr} = 0$. Then using our requirement that the reference profile appears at ϕ_0 in eq. (22) implies:

$$\theta_{corr}(r) = \frac{\left(\theta_v^{ref}(r)\right)^2}{\theta_v^1(r,\phi_0)} - \theta_v^{ref}(r). \tag{23}$$

https://doi.org/10.5194/wcd-2019-8
Preprint. Discussion started: 1 October 2019

Again, if eq. (18) were used, the small dependence of $H(r,\phi)$ on $\frac{\partial \ln \theta_v}{\partial r}$ could be dealt with by iteration but this proves unnecessary.

A first estimate of Exner pressure, Π^1 is then computed by integrating down from the model top:

$$\Pi(r,\phi) = \Pi_t + \int\limits_{r_t}^{r} \frac{B}{c_{pd}\theta_v(r,\phi)} \mathrm{d}r \tag{24}$$

where r_t is the model top and Π_t the Exner pressure there. This is then adjusted to make the surface pressure at the jet centre equal to the required surface pressure:

$$\Pi^1(r,\phi) = \Pi^1(r,\phi) + \Pi_s - \Pi^1(0,\phi_0) \tag{25}$$

Π_t is thus irrelevant and is set to zero in the code.

Overall, this procedure ensures that the reference surface pressure and θ_v profile result at the jet centre, while the θ_v and Π fields satisfy quasi-hydrostatic and thermal wind balance.

PE use a reference profile given by

$$T_r(z) = T_0 + \frac{\Gamma_0}{\left(z_T^{-\alpha} + z^{-\alpha}\right)^{1/\alpha}}, \tag{26}$$

with $T_0 = 300$ K, $\Gamma_0 = -6.5$ K/km, $z_T = 13$ km and $\alpha = 10$. This gives a constant dry lapse rate in the troposphere, transitioning smoothly to an isothermal layer in the stratosphere. Since Exner pressure is on a different level an iterative method is used to find a consistent integration of the hydrostatic relationship eq. (15) (with zero wind).

We use the more straightforward piecewise linear profile introduced by Baker et al. (2014):

$$\begin{aligned} \theta(z) =& \theta_0 + \Gamma_T z; && z \le z_T \\ =& \theta_0 + \Gamma_T z_T + \Gamma_S (z - z_T); && z > z_T \end{aligned} \tag{27}$$

with $\Gamma_T = 0.004$ K m^{-1}, $\Gamma_S = 0.025$ K m^{-1} and $z_T = 10^4$ m. Baker et al. (2014) use $\Gamma_S = 0.016$ K m^{-1} but that value would result in an unstable profile in the balanced thermal wind setup of this study, as explained below when describing the moisture profile.

The Baker et al. (2014) jet profile follows the approach of PE. We assume the jet is confined between ϕ_s and ϕ_e. Define

$$\begin{aligned} \phi^* =& 0 && ; \phi < \phi_s \\ =& \frac{\pi}{2}\frac{\phi - \phi_s}{\phi_e - \phi_s} && ; \phi_s \le \phi \le \phi_e \\ =& 0 && ; \phi_e < \phi \end{aligned} \tag{28}$$

Then

$$u(r,\phi) = u_0 F_\phi(\phi) F_r(r) + u_s G_\phi(\phi) G_r(r) \tag{29}$$

https://doi.org/10.5194/wcd-2019-8
Preprint. Discussion started: 1 October 2019

where

$$F_\phi(\phi) = \sin^3\left(\pi \sin^2 \phi^*\right) \tag{30}$$

$$F_r(r) = \left(\frac{z}{z_T}\right)^\gamma \exp\left\{\delta\left[1 - \left(\frac{z}{z_T}\right)^{\frac{\gamma}{\delta}}\right]\right\} \tag{31}$$

$$G_\phi(\phi) = \sin^2(2\phi)\left(\frac{\phi - \phi_{sh}}{\Delta\phi}\right)\exp\left[-\left(\frac{\phi - \phi_{sh}}{\Delta\phi}\right)^2\right] \tag{32}$$

$$G_r(r) = \frac{z}{z_s} \tag{33}$$

$z = r - r_0$, r_0 is r at the surface, z_T is the height of the tropopause above the surface, ϕ_{sh} is the latitude of the centre of the shear, $\Delta\phi$ the latitudinal width of the shear, z_s is the scale height of the shear, u_0 is the strength of the jet and u_s provides a meridional shear and, thus, non-zero u_s is used to setup an LC2 base state.

PE use $\phi_s = 0°$N, $\phi_e = 90°$N (so the jet centre is at $\phi_c = 45°$N), $z_T = 1.3 \times 10^4$ m, $u_0 = 45$ m s^{-1}, $u_s = 0$ m s^{-1}, $\delta = 0.5$ and $\gamma = 1$. We follow Baker et al. (2014) and use $\phi_s = 15°$N, $\phi_e = 85°$N (so the jet centre is at $\phi_c = 50°$N), $z_T = 10^4$ m, $u_0 = 45$ m s^{-1} (for the control run), $u_s = 0$ m s^{-1} (for an LC1 setup), $\delta = 0.2$ and $\gamma = 1$.

The moisture profile is specified in terms of a specified relative humidity field $RH(r,\phi)$. A complicating factor is that the calculation above has been performed in terms of θ_v, without knowing m_v. We adopt an iterative procedure to ensure that the correct RH profile is achieve while retaining the virtual temperature reference profile.

The RH profile is specified thus:

$$\begin{aligned} RH(r,\phi) =& RH_0\left[1 - 0.9R(\phi)\left(\frac{r - r_0}{z_T}\right)^\alpha\right] && ; r - r_0 \le z_T \\ =& 0.0625 RH_0 && ; z_T < r - r_0 \end{aligned} \tag{34}$$

with

$$\begin{aligned} R(\phi) =& 1.0 && ; \phi < \phi_s \\ =& 1 - 0.5 \times \frac{\phi - \phi_s}{\phi_e - \phi_s} && ; \phi_s \le \phi \le \phi_e \\ =& 0.5 && ; \phi_e < \phi \end{aligned} \tag{35}$$

The parameters chosen by Baker et al. (2014) produce a problem in the stratosphere; even though the RH is small, the temperature in the stratosphere is high enough that the calculated water vapour pressure is high enough to contribute substantially to the total pressure. The mixing ratio is thus very large (up to 0.4) resulting in low θ and, ultimately, a statically unstable profile. The model fails after about a day. Setting the initial m_v set to 10^{-8} above z_T helps, but we still have a statically unstable

https://doi.org/10.5194/wcd-2019-8
Preprint. Discussion started: 1 October 2019

layer. Since we are not very concerned with the precise value of stratospheric stability, we have re-run with $\Gamma_S = 0.025$ K m^{-1}. Using profile correction option 1 we obtain the initial state with a very weakly unstable layer in the stratosphere that runs stably for (at least) 10 days. Using profile correction option 2 we obtain the initial state shown in Fig. 1. This transfers the unstable layer to the tropical troposphere, but also runs stably for 10 days. If unperturbed, the jet remains essentially unchanged through this period, demonstrating that the initial setup is, indeed, well-balanced. The exception is the upper stratosphere, which does develop some small perturbations. However, these have no noticeable affect on the tropospheric flow. We assume that these perturbations arise from the approximation of eq. (18) to eq. (19), but have not verified this as it has no significant on the results.

To stimulate baroclinic growth, a small temperature perturbation is applied to the initial state following PE. The perturbation is independent of height and defined as

$$T'(\lambda,\phi) = T_p \cos(m\lambda)\,\mathrm{sech}^2\left[m(\phi-\phi_c)\right] \tag{36}$$

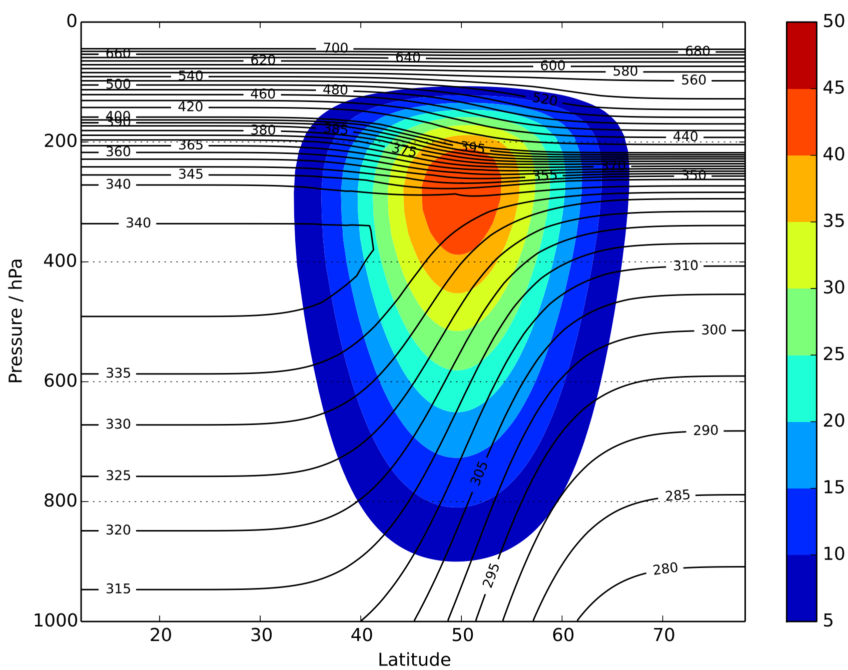

Figure 1. Initial potential temperature and U wind using setup according to Baker et al. (2014) but with $m_v = 10^{-8}$ in the stratosphere and $\Gamma_S = 0.025$, profile correction option 2. Note θ contour interval changes from 5 K to 20 K at 400 K.

where m is the wavenumber of the perturbation, ϕ_c = 50 °N is the latitude of the jet centre and T_p = 1 K. A wavenumber of $m = 8$ (consistent with the 45 °W–E extent of the model domain) is used in this study as in Baker et al. (2014), chosen to generate cyclones with a smaller length scale than those in Thorncroft et al. (1993) and PE (which used $m = 6$).

2.2 Mesoscale instability diagnostics

A primary focus of this paper is on the importance of mesoscale instabilities, dry ones in particular, for SJ generation. Mesoscale instabilities are detected following the method in Volonté et al. (2018), whose key points are repeated here. Diagnostics for each instability (labelling criteria in Table 1) are evaluated at each grid point and interpolated onto relevant trajectories (see Section 2.3). The two conditional instabilities (CI and CSI) contain an additional constraint of RH$_{ice} > 80\%$ (where RH$_{ice}$ is relative humidity calculated with respect to ice). This constraint is required because these instabilities can only be released if the air is saturated. The threshold of 80% is used because partial cloud formation occurs in the model when RH exceeds this threshold in the free troposphere. A grid point is labelled as stable only if none of the four diagnostic tests indicate instability. If instead diagnostic tests for CSI or CI indicate instability, but the saturation constraint is not met, the relevant grid point is not labelled as stable (S) and does not belong to any of the categories in Table 1. Every point can be labelled with more than one instability at the same time if two or more conditions are met. Our approach is to take the criteria as indicators of the underlying atmospheric state to highlight the processes leading to instabilities that might drive the dynamics of the SJ. These criteria are not used to indicate which instability might take precedence if more than one is present, particularly as they rely on assumptions about the background state upon which perturbations grow that are very rarely met in a highly baroclinic environment such as an intense extratropical cyclone. A more thorough discussion on the implications of this approach and on the relevant properties of PV (whose negative values are condition for symmetric instability) can be found in Section 2.3 of Volonté et al. (2018).

Label	${N_m}^2$	RH$_{ice}$	ζ_z	PV	MPV*
Conditional Instability (CI)	< 0	$> 80\%$			
Inertial Instability (II)			< 0		
Symmetric Instability (SI)				< 0	
Conditional Symmetric Instability (CSI)		$> 80\%$			< 0
Stable	≥ 0		≥ 0	≥ 0	≥ 0

Table 1. Criteria for trajectory instability and stability labels. ${N_m}^2$ is the moist Brunt-Väisälä frequency as defined by Durran and Klemp (1982). ζ_z is the vertical component of absolute vorticity (on pressure levels). PV is the potential vorticity and MPV* the moist saturated potential vorticity (Bennetts and Hoskins, 1979). Multiple entries in a row require all criteria to be satisfied (i.e. 'and' rather than 'or').

https://doi.org/10.5194/wcd-2019-8
Preprint. Discussion started: 1 October 2019

2.3 Trajectory analysis

The potential of Lagrangian trajectories to isolate airstreams and assess their properties and their time evolution has been extensively used in recent SJ research. Here, trajectories are computed using the LAGRANTO Lagrangian analysis tool (Wernli and Davies (1997); Sprenger and Wernli (2015)), as in Volonté et al. (2018). LAGRANTO uses an iterative Euler scheme with an iteration step equal to 1/12 of the time spacing of input data. Ideally, data every model time step would be used to compute the trajectories, but in practice some compromise is necessary to reduce the amount of required model output. For the idealised simulations analysed in this study it was found that trajectories computed with hourly input frequency of model data showed satisfactory conservation of relevant physical quantities; hence, all the results presented in this article use this input frequency.

2.4 Sensitivity experiments: motivation and configuration

The analysis of sensitivity experiments constitutes a substantial part of this study. As stated in the introduction, this analysis has been performed on a different set of parameters and range of parameter values to previous literature (Baker et al., 2014; Coronel et al., 2016) and is aimed at assessing the robustness of the occurrence of the SJ in intense Shapiro-Keyser extratropical cyclones, along with its strength and connection with mesoscale instabilities. The impacts of variations in model configuration and environmental parameters have been explored: model resolution, upper-tropospheric jet strength, sea surface temperature and initial state relative humidity (see Table 2).

Previous literature has shown the importance of adequate model resolution for a correct simulation of SJ dynamics (see section 4.3 of CG18 for an overview and Volonté et al. (2018) for a detailed discussion on the effect of instability generation along the SJ). Therefore, two simulations have been run with horizontal spacing increased from the 0.11° of the control run and with vertical resolution getting accordingly coarser (as shown in Table 2). The control value of the maximum initial relative humidity, $RH_0 = 80\%$ (see Eq. (34)), is the same as that chosen by Baker et al. (2014) to produce a profile similar to real soundings. Experiments were performed with increased and decreased RH_0 to provide an assessment of the influence of moisture content on the evolution of the cyclone and the associated SJ. These experiments are particularly relevant because moist processes occurring in the cloud head have a primary role in the evolution of the cyclone in which the SJ occurs and are instrumental in the SJ generation mechanism proposed in Volonté et al. (2018). Additionally, four experiments have been performed varying the strength of the jet-stream speed by changing its initial central value u_0 (see Eq. (29)) from the control value of u_0 =45 m s^{-1}. These experiments reveal the effects of different jet strength and, as a consequence, of different vertical wind shear and meridional temperature gradient.

A final set of experiments has been performed, but the results not included in this paper (although some results are presented in the PhD thesis by the lead author (Volonté, 2018)). This set consists of four experiments in which the physical latent heat constants of condensation and freezing are scaled by 0.75, 0.875, 1.125 and 1.25, following Büeler and Pfahl (2017). Whilst these experiments can help in assessing the effect of a variation in the intensity of diabatic processes and, as a consequence the effect of a changed static stability and resultant PV distribution, without changing the initial wind and temperature profile, their results are not presented for essentially two reasons. Firstly, changing the values of thermodynamical constants such as

https://doi.org/10.5194/wcd-2019-8
Preprint. Discussion started: 1 October 2019

325 these produces an unphysical situation with latent heat processes that are more or less intense than in the real world. Secondly, there is an inconsistency in the model as not all the variables can be updated according to the changes in these constants. In particular, the values of the specific humidity of saturation are taken from a look-up table, so they do not change if the value of the latent heat constants are changed, whereas all the thermodynamic quantities related directly or indirectly to those constants via an equation do. This generates a small inconsistency in the amount of cloud water, the effects of which are difficult to
330 quantify. Having been unable to solve these problems and acknowledging that the results from this set of experiments do not describe the behaviour of a realistic cyclone, we decided to not include them in this paper. However, we mention the attempt as in our opinion this method could become useful in future analyses if the aforementioned issues can be solved.

Experiment	horiz. grid spacing (°)	vertical levels	vert. spacing at 850 hPa (m)	u_0 (m s^{-1})	RH_0 (%)	T_0 (K)
control	0.11	70	140	45	80	295
025deg	0.25	63	200	45	80	295
04deg	0.4	38	360	45	80	295
rh90	0.11	70	140	45	90	295
rh70	0.11	70	140	45	70	295
jet35	0.11	70	140	35	80	295
jet40	0.11	70	140	40	80	295
jet50	0.11	70	140	50	80	295
jet55	0.11	70	140	55	80	295
t291	0.11	70	140	45	80	291
t293	0.11	70	140	45	80	293
t297	0.11	70	140	45	80	297
t299	0.11	70	140	45	80	299

Table 2. Table showing the parameter values chosen for the different experiments. Model top height is 40 km for all simulations. u_0 and RH_0 indicate, respectively, the maximum initial values of wind speed and relative humidity and the central initial value of surface temperature, as defined in Section 2.1.

https://doi.org/10.5194/wcd-2019-8
Preprint. Discussion started: 1 October 2019

2.5 Additional post-processing

The software NDdiag (Panagi, 2011) has been used to convert the model output to 15-hPa spaced pressure levels (30 hPa for the 04deg simulation) and to compute further diagnostic fields. All fields considered in this study, including conditions for instabilities (see Table 1), are thus on pressure levels. See Volonté et al. (2018) and Grams and Archambault (2016) for examples of the use of NDdiag in the literature.

System-relative speed has been computed by subtracting the average speed of the cyclone centre, i.e. its surface pressure minimum, from the Earth-relative wind speed of the trajectories. The average speed of the cyclone centre has in turn been computed after applying a 16-hour smoothing to the detected pressure minimum location. This choice is motivated by the need to remove irregularities in the location of the surface pressure minimum in all the different simulations while retaining genuine variations in the SJ speed relative to the motion of the cyclone centre. At the same time, system-relative speed is strongly dependent on the relative directions of the SJ and of the cyclone movement, and these can vary between different simulations and on different timescales. The time value for the running mean has thus been chosen empirically to obtain a system speed that is as consistent as possible between different simulations. System speed values go from 8.3 to 13.5 m s^{-1} in the simulations with modified initial jet-stream strength and stay within 10.9 and 12.4 m s^{-1} in all other simulations. Most of this variation is due to changes in zonal system speed, while meridional system speed ranges from 2.4 to 3.2 m s^{-1} in all simulations.

3 Results

3.1 Identification and characterisation of a SJ in the control simulation

3.1.1 Overview of the life-cycle of the storm

As discussed in the introduction, a necessary condition for the occurrence of a SJ is that the extratropical cyclone containing it evolves according to the Shapiro-Keyser conceptual model. Figure 2 confirms that the idealised moist baroclinic wave evolves according to this model by showing the time evolution of surface pressure and potential temperature, θ, at 850 hPa throughout the main stages in the control simulation. At 72 hours from the start of the run the cyclone is in its initial stage of development (Figure 2a), with meridional advection associated with the growing disturbance. At 84 hours (Figure 2b) the foremost part of the warm advection is now westward relative to the cyclone centre as the cyclone evolves towards a frontal 'T-bone' structure with the development of a bent-back front and the opening of a frontal-fracture region to the south of the cyclone centre, an area with intermediate θ values (between 295 K and 300 K) and weak gradients of θ (and of θ_w, not shown). At 96 hours (Figure 2c) the bent-back front is fully developed and the associated cold advection is starting to close the frontal-fracture region and isolate a warm seclusion at the centre of the cyclone. The cyclone is now deeper, with the minimum surface pressure below 970 hPa, 12 hPa less than 12 hours before. At 108 hours (Fig. 2d) the warm seclusion is almost completely encircled by the wrapped-up bent-back front, in what resembles a mature stage of evolution of a Shapiro-Keyser cyclone gradually losing its baroclinic nature. The evolution just described follows the four stages of the Shapiro-Keyser model, correctly displaying its main features

https://doi.org/10.5194/wcd-2019-8
Preprint. Discussion started: 1 October 2019

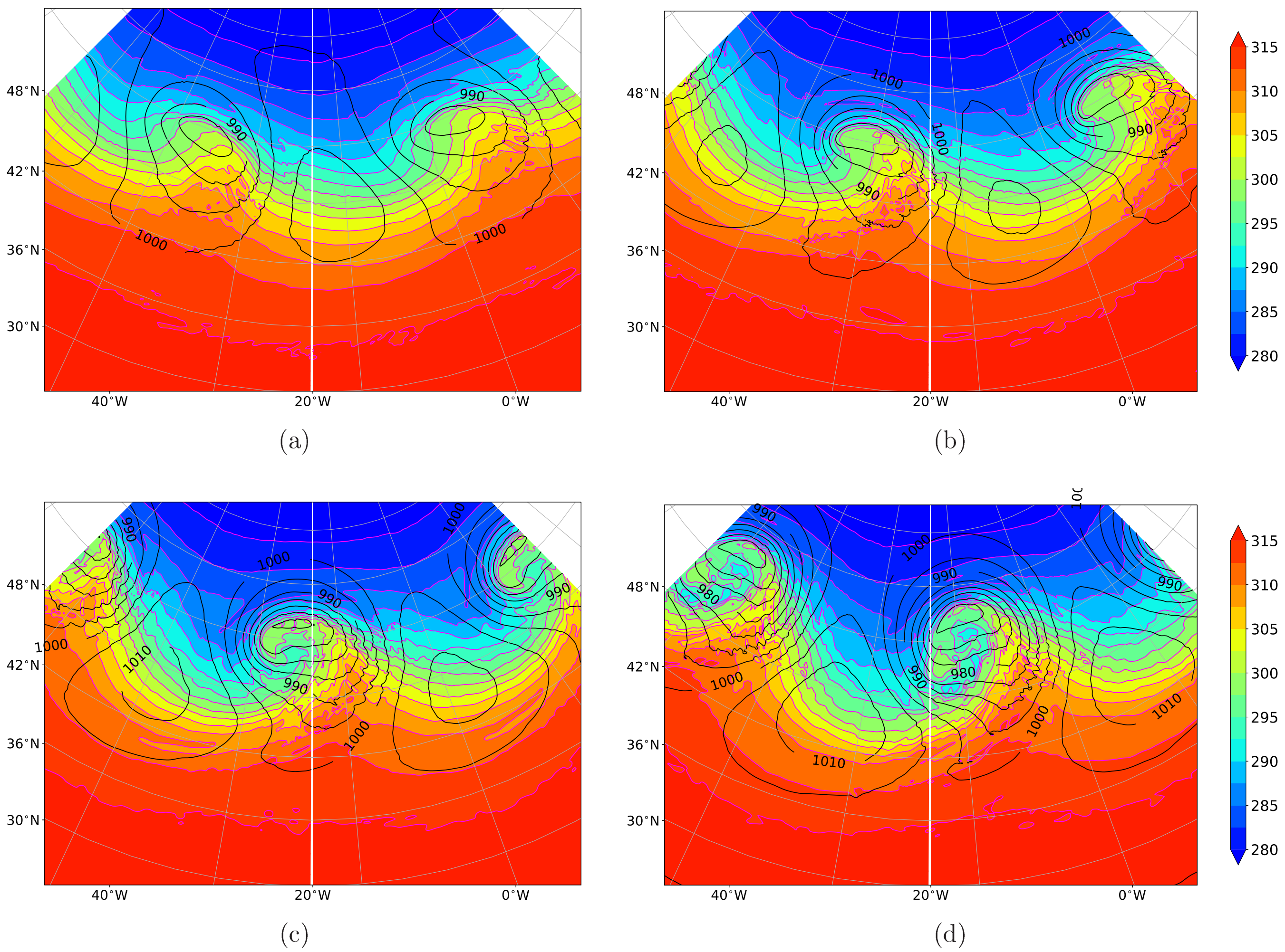

Figure 2. Surface pressure (black contours, hPa) and θ at 850 hPa (colours and magenta lines, K) after (a) 72, (b) 84, (c) 96 and (d) 108 hours from the start of the control simulation. Note that the model domain (whose original zonal extension goes from 20°W to 25°E with periodic E-W boundary conditions) is repeated zonally to facilitate visualisation.

in time and space. In particular, it is between 84 and 96 hours from the start that the cyclone displays a widening frontal fracture, resembling a typical Shapiro-Keyser cyclone in Stage III of its development (Shapiro and Keyser, 1990). Hence, it is in that time range that the descent of a SJ can be expected to take place in the frontal-fracture region (CG18).

3.1.2 Analysis of strong winds in the frontal-fracture region

Figure 3 shows that strong low-level winds in the frontal-fracture region can indeed be clearly identified in the control simulation during stage III of the cyclone evolution. At 94 hours from the run start, Fig. 3a displays a wind-speed maximum exceeding 35 $\mathrm{m\,s^{-1}}$ at 850 hPa that is located in the frontal-fracture region characterised by weak θ_w gradients. This region is

https://doi.org/10.5194/wcd-2019-8
Preprint. Discussion started: 1 October 2019

Weather and Climate Dynamics Discussions
Open Access

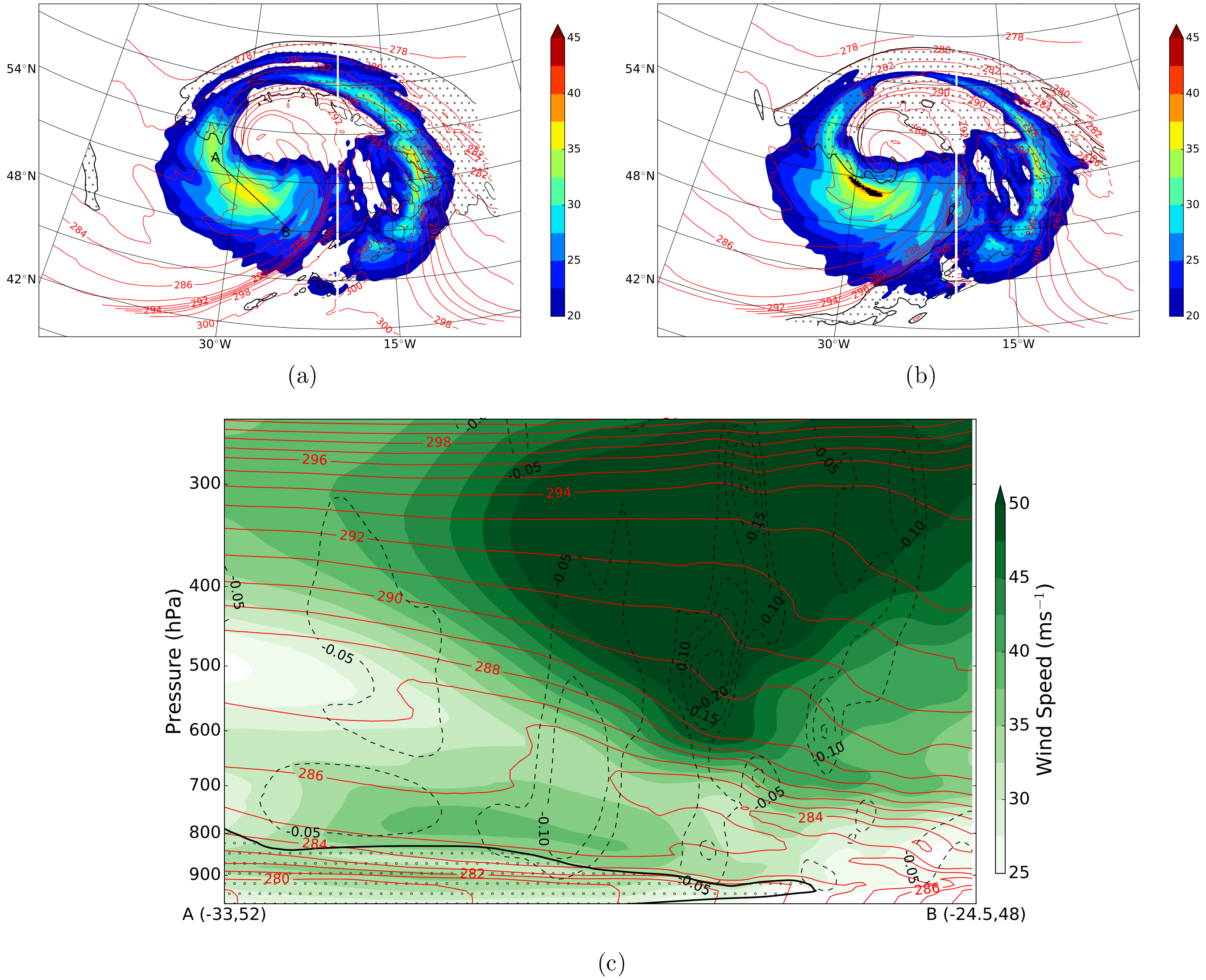

Figure 3. (a) Wind speed at 850 hPa (contours, m s^{-1}), θ_w at 850 hPa (K, red lines) and cloudy regions at 700 hPa (RH$_{ice}$ >80%, black lines and dotted regions) after 94 hours from the start of the control simulation (as all the other panels in this figure). Note that the model domain (whose original zonal extension goes from 20°W to 25°E with periodic E-W boundary conditions) is repeated zonally to facilitate visualisation but only data between 45°W and 5°W are shown here. (b) Same as (a) but at 805 hPa for all fields. Black dots show the horizontal locations of SJ trajectories. (c) Cross section (transect AB in panel (a)) of wind speed (green filled contours), negative vertical velocity (dashed black lines, m s^{-1}), θ_w (red lines, K) and cloudy regions (RH$_{ice}$ >80%, thick black lines).

just south of the cyclone centre, and lies behind an intense cold front ($\Delta\theta_w$ ~10 K across the less-than-100 km width of the front) and ahead of the cloud-head tip and the associated bent-back front, partially wrapped around the cyclone centre. The cloud-head tip at 700 hPa displays some waviness, consistent with the occurrence of cloud banding and slantwise convection.

https://doi.org/10.5194/wcd-2019-8
Preprint. Discussion started: 1 October 2019

The location of this wind maximum is thus consistent with the descent of a SJ. Other low-level strong-wind regions of similar or even larger magnitude can be found elsewhere (see in the same figure the elongated strong-wind region running along the warm front, locally up to 35 m s^{-1}, associated with the warm conveyor belt) and/or at later times. The strongest wind speeds at 850 hPa in the whole lifetime of the storm, close to 40 m s^{-1}, occur at around 120 hours and are associated with the cold conveyor belt when the storm is in its mature stage (not shown). As this work is focused on the evolution of SJs in idealised extratropical cyclones, other low-level strong-wind features will not be examined.

The core of the SJ-associated wind maximum is located around 800 hPa, as shown in Fig. 3b. The black dots overlaid on the wind-maximum region indicate the starting points of the Lagrangian trajectories selected to represent the core of this airstream. The selection has been performed by using only a constraint on Earth-relative wind speed at a specific time, i.e. by identifying the 100 grid points with highest wind speed at 94 hours from the run start located at 805 hPa or in contiguous levels (i.e. aligned vertically with the grid points selected at 805 hPa to form uninterrupted columns of points with speed exceeding the threshold). All these points have a wind speed exceeding 38.51 m s^{-1} and they are all located between 760 and 820 hPa in a compact area in the core of the wind maximum visible in the frontal-fracture region, just ahead of the cloud-head tip.

A cross section taken along the frontal-fracture region (Fig. 3c, transect AB in Fig. 3a) shows an evident fold in θ_w embedded in an area of weak θ_w gradients, underneath a more stable layer of downward-sloped isentropes in the middle troposphere. The low-level wind maximum described in the previous paragraphs can be clearly identified in this cross section, located along the base of the θ_w-fold, surrounded by regions of negative vertical velocity and with speed values close to 40 m s^{-1} at its core, at around 800 hPa. This wind maximum sits on top of the saturated boundary layer, neutral to slightly conditionally unstable in its lower part and capped by a strongly stable layer. The boundary layer also contains a low-level jet around 900 hPa, with wind speed up to 35 m s^{-1}, that is possibly associated with the front edge of the cold conveyor belt. The situation depicted by Fig. 3 is consistent with the description of SJ-associated wind maxima in previous studies (listed in Table 3 in CG18). In particular, this can be compared with Fig. 4 in Volonté et al. (2018); the structure is very similar, even though the SJ reaches higher wind speeds, up to 60 m s^{-1}, in that case. and see the list of other studies).

Lagrangian trajectories are used in the next sections to assess the characteristics of the identified SJ, following the steps outlined in Volonté et al. (2018).

3.1.3 Analysis of relevant quantities on the SJ airstream

Figure 4 shows the time evolution of various physical quantities along the trajectories identified as the SJ core, with dashed vertical lines highlighting key times in their evolution: 82, 88 and 94 from the start of the run. These times indicate respectively (and somewhat subjectively): (1) the start of the increase in SJ speed in both Earth-relative and system-relative reference frames; (2) the start of more rapid SJ descent and the end of the main increase in system-relative speed; and (3) the end of the increase in Earth-relative SJ speed, at the time of SJ detection. The steady increase in wind speed experienced by the airstream between (1) and (3) is displayed in Fig. 4a, with maximum values close to 40 m s^{-1}. Before (1) the various trajectories span wind speeds between 5 and 30 m s^{-1}, the range at least partially a consequence of different paths taken by the air parcels as

https://doi.org/10.5194/wcd-2019-8
Preprint. Discussion started: 1 October 2019

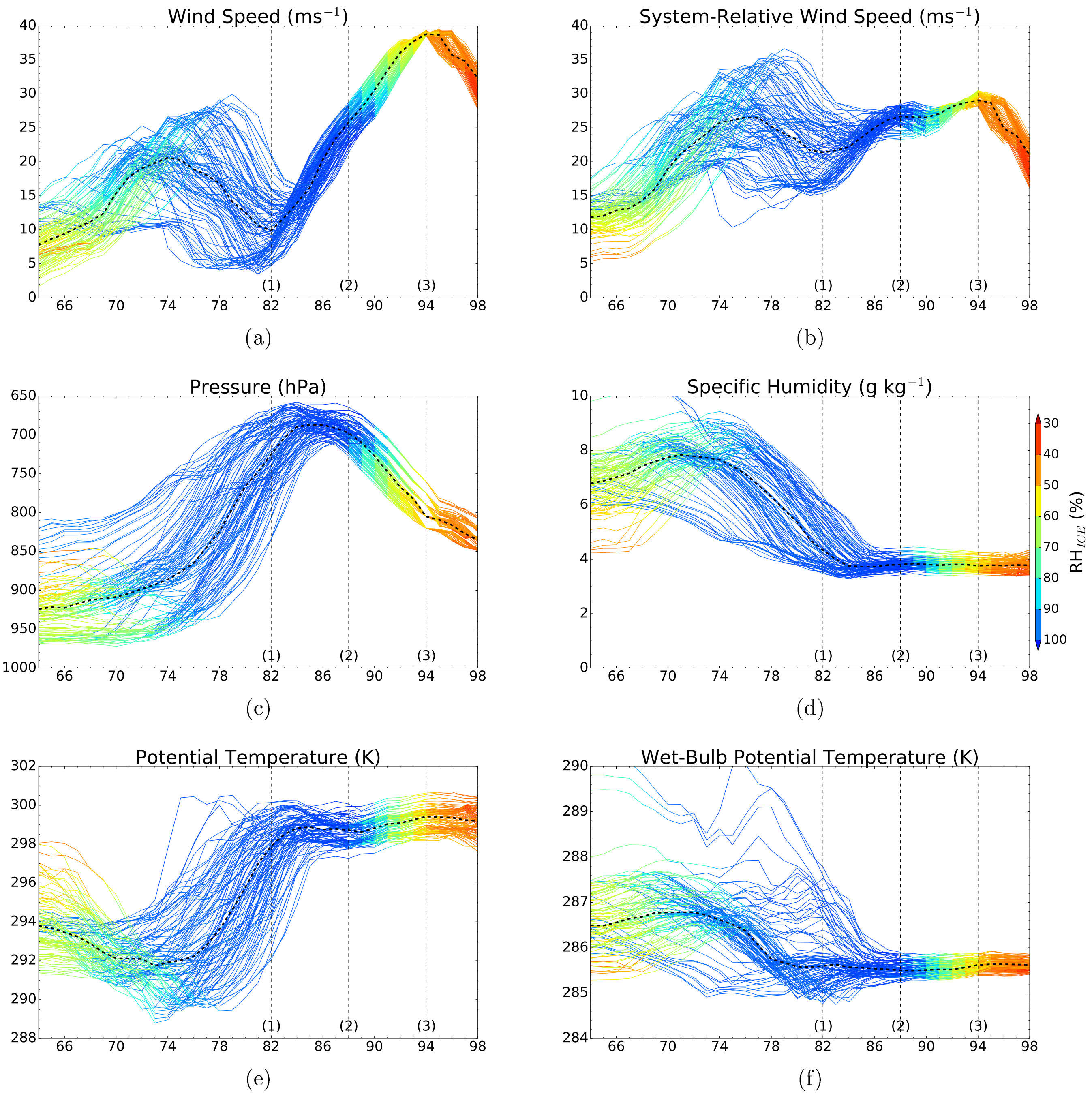

Figure 4. Timeseries (hours since start of the run) of (a) wind speed, (b) system-relative wind speed, (c) pressure, (d) specific humidity, (e) potential temperature and (f) θ_w along SJ trajectories. Colours indicate relative humidity with respect to ice along trajectories and the dashed line indicates the median of trajectories.

https://doi.org/10.5194/wcd-2019-8
Preprint. Discussion started: 1 October 2019

they travelled around the cyclone centre. Some markedly reduce their speed, by up to 20 $\mathrm{m\,s^{-1}}$ before reaching their peak altitude and starting descent.

Conversely, during their increase of wind speed all trajectories behave coherently, with the median value of trajectories increasing in speed by almost 30 $\mathrm{m\,s^{-1}}$, indicating that acceleration of a single coherent airstream is occurring, i.e the SJ. Part of this acceleration is due to the SJ rotating around the cyclone centre and moving eventually in the same direction of the overall motion of the cyclone when on its southern side. This effect is not present in Fig. 4b, which shows wind speed in a system-relative reference frame, i.e. having subtracted the motion of the storm (mainly zonal) from the Earth-relative wind. Nevertheless, this figure shows that system-relative wind speed increases by about 5 $\mathrm{m\,s^{-1}}$ for the median of trajectories between (1) and (2). For approximately 1/3 of the trajectories the coherent increase in system-relative wind speed in the same period reaches 10 $\mathrm{m\,s^{-1}}$. It must be acknowledged that a substantial minority of the trajectories undergo little or no speed increase or even a slow-down between (1) and (2). Between (2) and (3) the trajectories are a much more coherent bundle and generally experience further small but positive speed increment, the median increasing by 2-3 $\mathrm{m\,s^{-1}}$. These values, although substantially smaller than the $\sim$15 $\mathrm{m\,s^{-1}}$ calculated for windstorm Tini in Volonté et al. (2018), indicate a non-negligible local speed increase of the SJ that is not related to the overall motion of the storm.

Figure 4c shows that the trajectories form a coherent bundle after they start their descent (or, more accurately, as they are back trajectories, start to lose their coherency as they extend back in time from the start of their descent). Their increase in Earth-relative wind speed occurs at the same time as a steady descent. The median SJ trajectories increase their median pressure by 108 hPa in 6 hours, moving from 697 to 805 hPa between (2) and (3), during the most rapid stage of their descent. After (3) the descent gets weaker, as the SJ starts decelerating. This descent comes after an earlier ascent in which different populations of trajectories, mainly starting below the pressure level of 850 hPa, merge into a single airstream located around 700 hPa. Again, the magnitude of this descent is consistent with results from previous studies, although smaller than the 150 hPa in 3 hours in windstorm Tini (see Fig. 6 in Volonté et al. (2018)).

The descent of the SJ is also associated with a decrease in relative humidity, from close to saturation down to 40% in less than 10 hours. Figure 4d shows that during this drying stage specific humidity stays nearly constant at around 4 $\mathrm{g\,kg^{-1}}$ with only an almost negligible increase, of around 0.1 $\mathrm{g\,kg^{-1}}$ for most trajectories, in the first part of the descent up to (2). Throughout the ascent instead, all the trajectories stay close to saturation, with specific humidity substantially decreasing for all trajectories (from nearly 8 $\mathrm{g\,kg^{-1}}$ to less than 4 $\mathrm{g\,kg^{-1}}$) after an initial increase.

Figures 4e and 4f confirm the absence of any clear evaporative — or sublimational — cooling signal during the descent of the SJ (in fact θ_w variations do not exceed 0.15 K for most trajectories in the whole descent) and the presence of condensational heating during the ascent, with a median increase in θ of around 7 K over 10 hours. This overall behaviour implies the occurrence of substantial condensation and precipitation while the SJ ascends within the cloud head whereas the amount of evaporation during descent is at least an order of magnitude smaller.

The limited variations in θ_w for most SJ trajectories from the final part of the ascent and throughout all the subsequent evolution indicate also the accuracy of the trajectories computed (as θ_w is expected to be conserved in absence of radiative and ice processes, and mixing), confirming the 'single coherent airstream' behaviour. This is opposed to the large variations, up to

https://doi.org/10.5194/wcd-2019-8
Preprint. Discussion started: 1 October 2019

a few K, happening particularly by the beginning of the ascent where different populations of trajectories merge before starting to travel together along a narrow frontal zone. Hence, these trajectories can be safely considered representative of the motion of the SJ as a coherent airstream only from halfway through the ascent, when the variations in θ_w to the end of the descent reduce below 1 K. This early lack of coherency does not affect the usefulness of the trajectories for this work as it is during the second part of the ascent and throughout the descent of the SJ that the dry mesoscale instabilities occur along the jet (see Section 3.1.4).

It must be remembered that these are back-trajectories computed from time (3); as already mentioned, they form a very well-defined and coherent structure almost to the start of their descent. We interpret the relative lack of coherency before this as arising from the fact that the air at the start of its descent is within the very tight gradient of the frontal zone in the cloud head. This tight gradient leads to mixing, which may be a combination of numerical artefact from the trajectory calculation and real shear-induced mixing. The broad picture of ascent and potential warming by condensation heating prior to descent is likely to be reliable, but detail such as changes in horizontal speed less so. This is a limitation of the trajectory technique, not of the model, though of course the treatment of mixing at the frontal boundary in the model may also have some relevance.

In summary, the identified SJ shows an ascent-descent pattern that is consistent with most previous studies, although less intense than the one in windstorm Tini. The rate of the descent reaches values around 20 $\mathrm{hPa\,hr^{-1}}$ for 5 consecutive hours. This descent is associated with a substantial increase in wind speed with values up to 40 $\mathrm{m\,s^{-1}}$ and exceeds by at least 5 and possibly up to 10 $\mathrm{m\,s^{-1}}$ the increase in wind speed due to the motion of the SJ in relation to the overall system motion. The occurrence of condensation during the ascent of the SJ airstream is evident while any contribution of evaporative/sublimational cooling at the start of the descent is small.

3.1.4 Evolution of mesoscale instabilities along the airstream

Figure 5 shows the time-pressure profile of the SJ airstream overlaid on bars representing the percentage of trajectories unstable to different instabilities at each time, allowing us to assess the evolution of instabilities on the airstream. In the hours preceding the ascent and then descent of the SJ the number of trajectories unstable to CSI increases up to a temporary maximum exceeding 60%. At the same time the number of trajectories unstable to SI gets close to 40%. As documented in Section 3.1.3, the evident non-conservation of θ_w during this period does not allow us to consider the bundle of SJ trajectories as a single coherent airstream. Nevertheless, the large numbers of points where instability to CSI and SI is detected indicates the occurrence of widespread areas with negative MPV* and PV, respectively. In these early hours the number of trajectories unstable to II is smaller than to SI, see for example at 74 hours from the start. Moist static instability is almost negligible, as indicated by the lack of CI; consequently dry static instability is also negligible. Hence, a negative sign of PV in locations where ζ_z is not negative (i.e SI in the absence of II) does not come from a negative value of static stability but from negative values of the horizontal components of $\zeta \cdot \nabla\theta$, indicating a very tilted environment in terms of momentum— and θ— surfaces. During the second part of the ascent of the SJ (where it can be considered a single coherent airstream) there is a second build-up of SI and II, both exceeding 30% of trajectories at 83 hours and just exceeding the value for CSI. As the SJ reaches the top of its ascent and then starts the subsequent descent, the values steadily decrease for all these instabilities until the all the trajectories

https://doi.org/10.5194/wcd-2019-8
Preprint. Discussion started: 1 October 2019

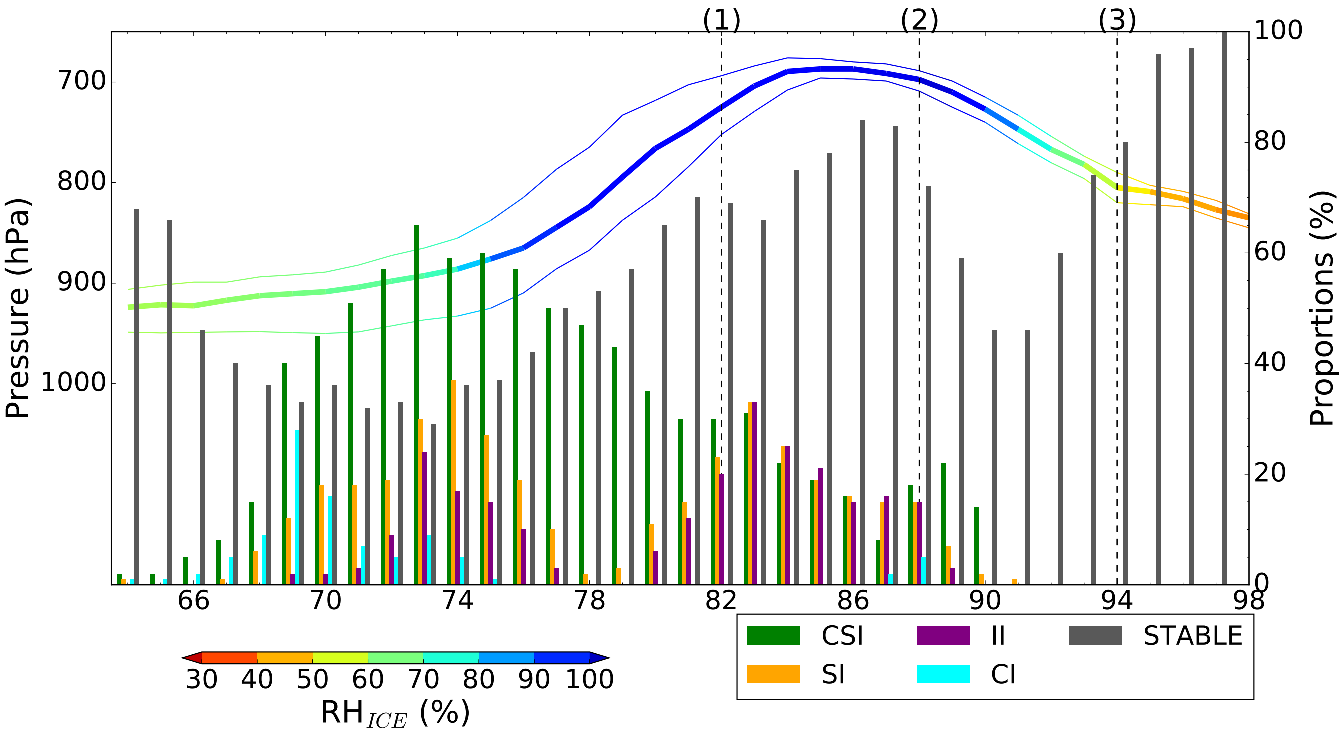

Figure 5. Timeseries (hours since start of run) of pressure (colours indicate relative humidity w.r.t. ice) and diagnosis of instability conditions along the trajectories in coloured bars. See section 2.2 for details on instability diagnostics.

become stable. The maximum number of trajectories unstable to dry mesoscale instabilities in the ascended SJ is substantially smaller than in the results of Volonté et al. (2018), where up to 75% of the trajectories of the SJ in the simulation of windstorm Tini were labelled as unstable to SI and II. However, the evolution depicted does suggest that the release of dry mesoscale instabilities such as SI and II takes part in the dynamics of SJ speed increment and descent.

3.1.5 Evolution of potential vorticity in the cloud head

Figure 6 displays the evolution of PV at the tip of the cloud head and the associated location of trajectories between 83 and 91 hours from the run start, to investigate the location and extent of unstable regions and their relation to the SJ. The pressure level chosen for each panel is that closest to the median pressure of the SJ trajectories at that time. Figure 5 shows that up to ~30% of the SJ trajectories become unstable to SI just before starting to descend, at around 83 hours, while Fig. 6 displays the time evolution of SI along the trajectories from that time onwards. Elongated regions of negative PV travelling along the frontal zone, just on its outer side, associated with the warm, and then bent-back, front can be seen in all panels. The front is indicated by high PV values, a consequence of large positive values in ζ_z, due to the across-front horizontal wind shear, and a tight horizontal across-front gradient in θ_w. The SJ trajectories travel around the front within the cloud head, along the same path on which the localised regions of negative PV move. When the SJ then reaches the banded tip of the cloud head and exits

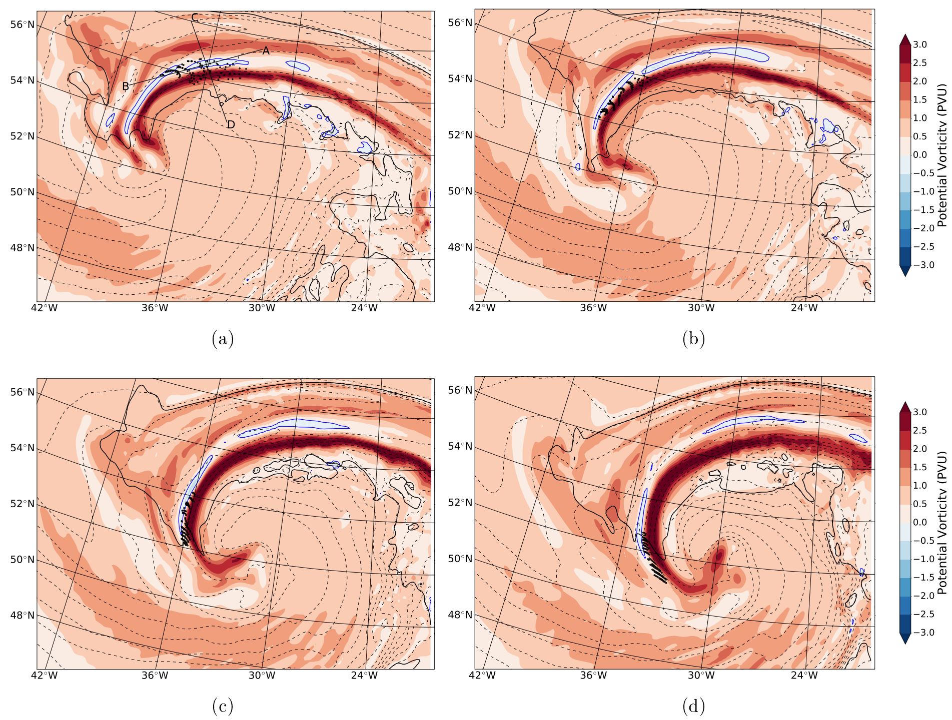

Figure 6. PV (shading, PVU), θ_w (thin dashed contours every 1 K) and cloudy regions (RH$_{ice}$=80%, black solid contours) at (a) 700 hPa at 83 hours from run start, (b) 685 hPa at 86 hours, (c) 715 hPa at 89 hours, (d) 745 hPa at 91 hours. Black dots show the locations of the trajectories.

from it starting to descend, the negative values of PV gradually disappear, suggesting a release of SI via the slantwise descent experienced by the SJ trajectories.

Figure 7 shows two cross sections, one along-flow and one across-flow, taken at 83 hours from the run start, i.e. at the time during the SJ ascent when the number of SI-unstable trajectories is maximum. The transects of the sections are marked in Fig. 6a. The along-flow section (Fig. 7a) shows a band of negative PV centred at around 300 km from point A, located just below 700 hPa and slightly downward tilted. Some of the trajectories travel within this band, forming the 30% SI-unstable subset of the airstream already mentioned. Note that some other trajectories are located ahead of this band, somewhat closer to the tail of other bands of negative PV that extend to the tip of the cloud head (Fig. 6a). In general, the presence of several localised regions with values of PV close to zero or negative suggests that the area close to the bent-back front in the cloud head represents a favourable environment for the existence of SI (or at least reduced symmetric stability). The across-flow section (Fig. 7b) instead highlights the slantwise tilted dipole of PV located along the narrow frontal zone in which the SJ travels, at around 700 hPa and between 150 and 225 km from point C. This pattern suggests the occurrence of ascending and descending slantwise motions orientated with the slope of the frontal zone, an hypothesis that is confirmed by Fig. 8, whose panels show the zonal and meridional components of relative vorticity, respectively. The two panels of Fig. 8 highlight the presence of

https://doi.org/10.5194/wcd-2019-8
Preprint. Discussion started: 1 October 2019

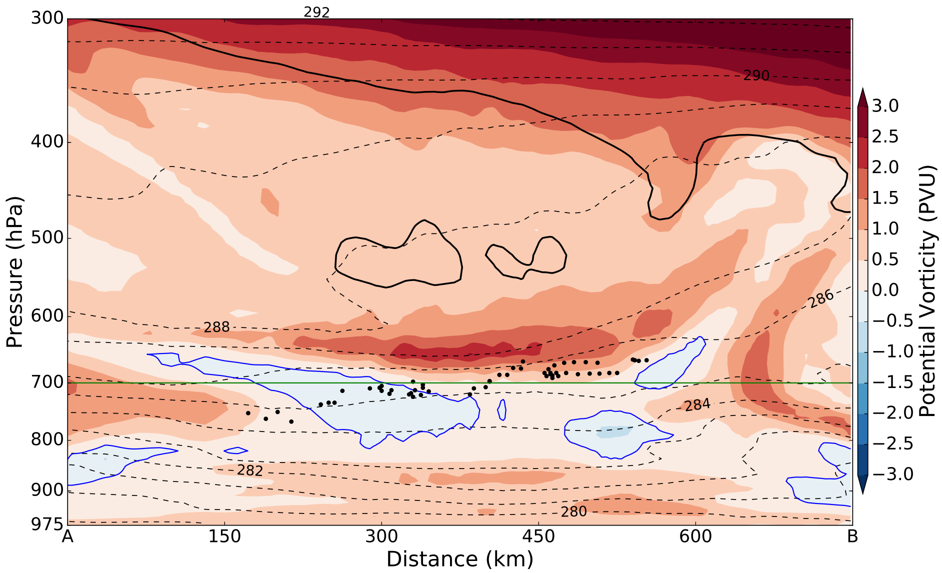

(a)

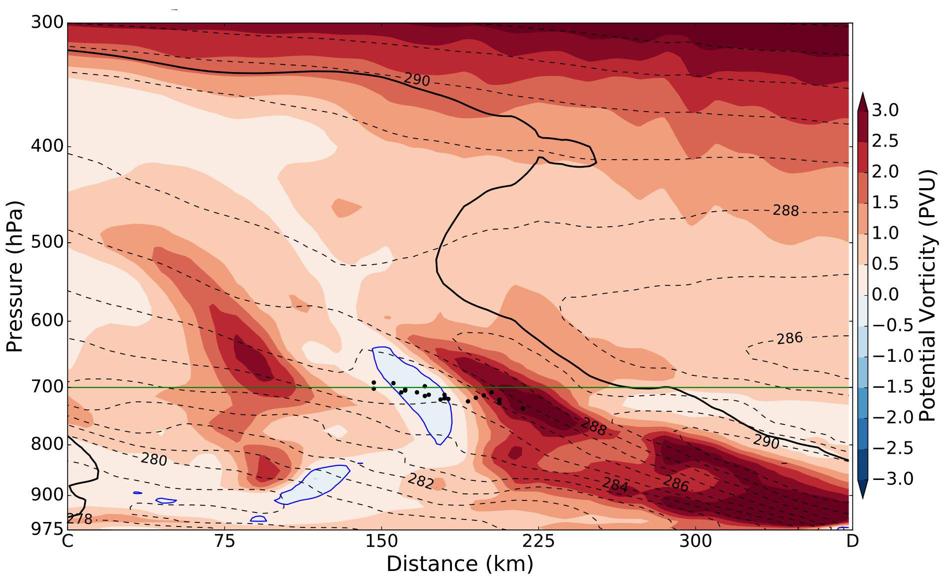

(b)

Figure 7. Cross sections on transect (a) AB and (b) CD of Fig. 5a of PV (shading), θ_w (thin black dashed contours, K) and cloudy regions (RH$_{ice}$=80%, black bold contours) at 83 hours from run start. Black dots show the perpendicular projection on the transect of the trajectories that are less than 25 km distant from the relevant transect. The green line indicates the pressure of 700 hPa, to which to which Fig. 6a refers.

slanted vorticity dipoles and tripoles, in the region of the SJ trajectories, that are direct consequence of the slantwise ascent-

https://doi.org/10.5194/wcd-2019-8
Preprint. Discussion started: 1 October 2019

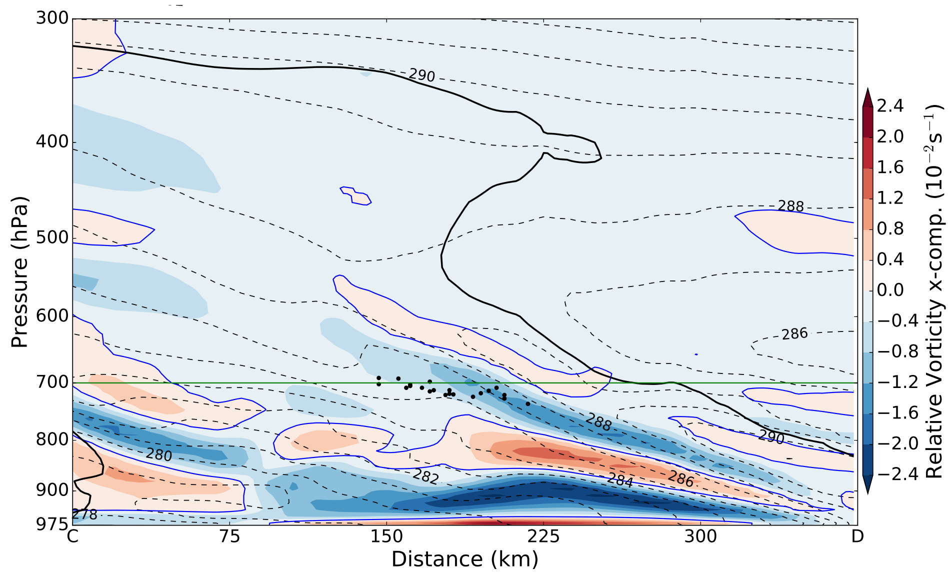

(a)

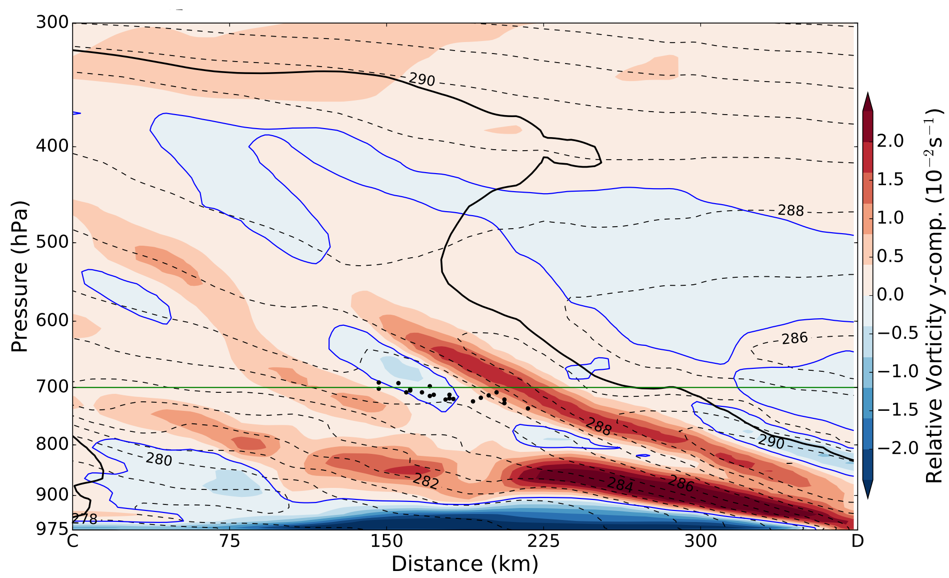

(b)

Figure 8. Cross sections on transect CD of Fig. 5a of (a) zonal and (b) meridional components of relative vorticity (shading), θ_w (thin black dashed contours, K) and cloudy regions (RH_{ice}=80%, black bold contours) at 83 hours from run start. Black dots show the perpendicular projection on the transect of the trajectories that are less than 25 km distant from the relevant transect. The green line indicates the pressure of 700 hPa, to which Figure 6a refers.

over-descent pattern along the frontal zone. In detail, negative values of the zonal and meridional components of vorticity encircled by positive bands are compatible with ascent on the southern and western side of the frontal surface, respectively, and a descending return circulation on its other side. This pattern is visible for both components, indicating the occurrence of a slantwise direct frontal circulation, with ascent on the southwestern side of the front. This overall situation is consistent with the mechanism, outlined in Volonté et al. (2018), of generation of negative horizontal vorticity, that can be eventually tilted into negative ζ_z to trigger II (and SI too if, as a consequence and as is the case here, also PV decreases below zero).

In summary, the analysis presented in this section indicates the presence of localised regions of negative PV created in the cloud head, where slantwise motions occur along a narrow frontal zone. These regions move towards the cloud-head tip and can be associated with a jet that, travelling within that frontal zone, descends and accelerates while the negative PV ceases to be present. Overall, the evolution of the SJ airstream identified in the control simulation and its association with the evolution of mesoscale instabilities follows the results and the conceptual model presented in Volonté et al. (2018), despite the expected differences in magnitude and timing.

3.2 Sensitivity experiments

3.2.1 Aim and overview

In the previous section it was shown that mesoscale instabilities (conditional and dry) play an active role in the evolution of the SJ in the control simulation. We now assess the robustness of the occurrence of the SJ, along with its strength and connection with mesoscale instabilities, through the sensitivity experiments described in Section 2.4.

All the simulations display a baroclinic wave evolving according to the Shapiro-Keyser conceptual model (not shown), similar to the evolution shown in Fig. 2 for the control simulation. There is variability between experiments in the intensity of fronts and in the shape and size of cloud head and frontal-fracture region, particularly in runs where the initial temperature has been modified (not shown). However, in all simulations it has been possible to identify a low-level (i.e. between 700 an 850 hPa) wind maximum located in the frontal-fracture region (outside the cloud head and above the stable and moist boundary layer) at the time of its widening. Consequently, 100 contiguous grid points have been selected in each run as starting points for the SJ trajectories, following the same procedure used for the control simulation i.e. points contiguous with an Earth-relative wind-speed maximum located close to an area of θ_w-folding in the frontal-fracture region and above the almost-saturated boundary layer; these trajectories tentatively represent the SJ cores. For most experiments the SJ is detected around 93-96 hours from the start of the run. The only simulations showing a markedly different speed of cyclone development and therefore an earlier or later time of SJ identification are the ones with a modified strength of the upper-tropospheric jet: for example an increase of the initial jet speed of 5 $\mathrm{m\,s^{-1}}$ is associated with an earlier onset of the SJ descent by about 10 hours, and vice versa.

https://doi.org/10.5194/wcd-2019-8
Preprint. Discussion started: 1 October 2019

3.2.2 SJ evolution

The airstreams tentatively identified as SJs in the different runs show several common characteristics. However, by dividing them in two subsets it is easier to detect noticeable differences in their behaviour. Time series of pressure, wind speed, PV and MPV* along the SJ trajectories for each run are shown in Figs. 9 and 10 for the respective subsets of (i) experiments with SJs displaying most of the variability (control simulation plus the runs where jet-stream strength and model resolution have been modified) and (ii) the remaining experiments (control simulation plus the runs where initial surface temperature and relative humidity have been modified).

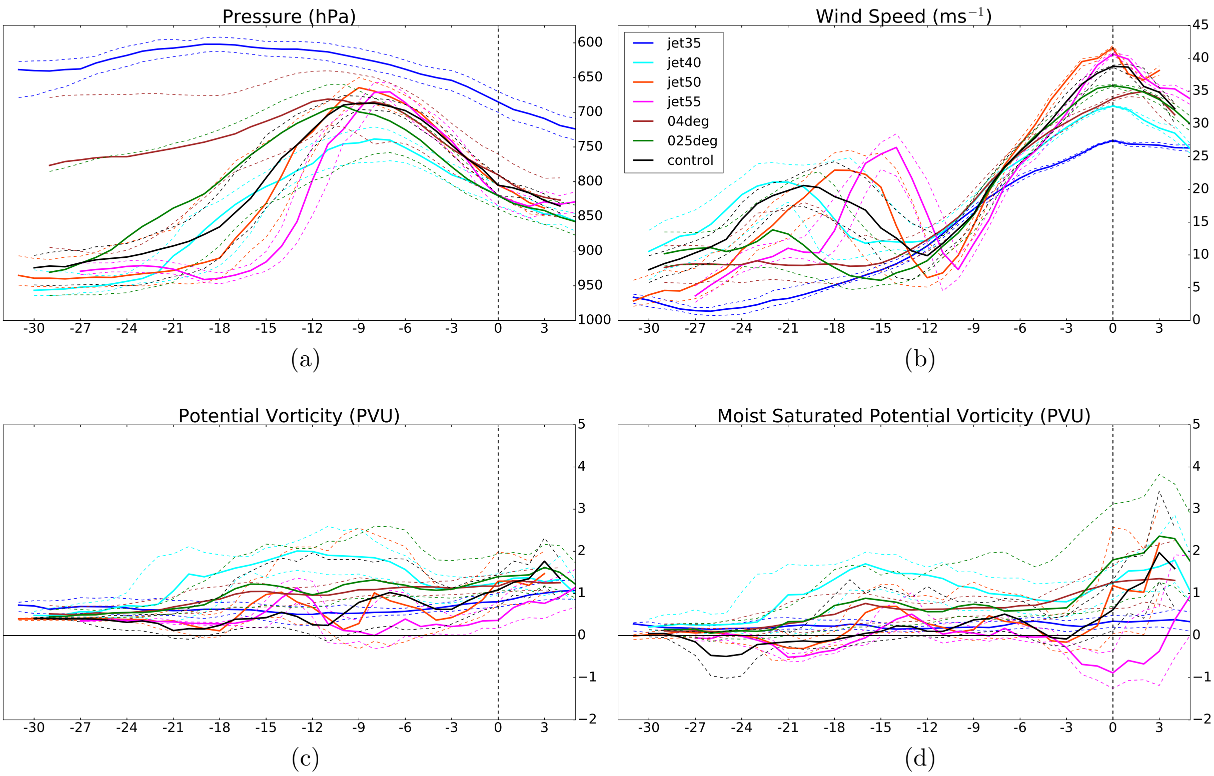

Figure 9. Timeseries (hours relative to the time of identification of each airstream) of (a) pressure, (b) wind speed, (c) PV, (d) MPV* along SJ trajectories for the control simulation and for the runs with modified jet stream (jet35, jet40, jet50, jet55) and model resolution (025deg, 04deg). Solid lines indicate the median values of each set of trajectories and dashed lines indicate 25th and 75th percentile values.

Figure 9a shows that in all but one of the simulations the median values of trajectories are located close to 800 hPa at the time of identification, towards the end of their strong descent. The exception is the jet35 run, in which the descent is much weaker and the median of trajectories is around 700 hPa at that time; we later conclude that the airstream identified in jet35 cannot be classified as a SJ. This airstream also does not display an initial ascent (although this is not a requirement for the

https://doi.org/10.5194/wcd-2019-8
Preprint. Discussion started: 1 October 2019

classification as a SJ), whereas a marked ascent-descent pattern can be identified for the SJ airstreams in all other runs. Median values of trajectories generally rise from below 900 hPa to around 700–750 hPa before descending back to around 850 hPa. The ascent rate of the SJ prior to its descent decreases with decreasing model resolution, particularly noticeable for the 04deg run for which the median of trajectories never exceeds 800 hPa in its early stages and the spread of ascent rates (as shown by the quartile trajectories) is largest. The SJs showing the largest ascent and descent rates are those with the enhanced jet strength: those in the jet50 and jet55 runs. Their second part of ascent and first part of descent are faster than for other SJs, with a total descent around 30–40 hPa larger than for the other SJs. The analysis of the evolution of relative and specific humidity and of θ and θ_w (not shown) reveals that these SJs go through an evolution that is similar to that described in Section 3.1.3 for the control run. All selected airstreams (apart from that in jet35) show some initial evaporation/sublimation occurring on the trajectories, prior to the formation of coherent airstreams, followed by saturated ascent in the coherent airstream associated with condensation and precipitation and then an almost-adiabatic descent during which moist processes are absent or negligible (not shown).

The associated evolution of wind speed is shown in Fig. 9b. Most of the SJs show a clear oscillation in wind speed centred at around 15 hours before the identification time. This oscillation is associated with the airstreams turning around the cyclone centre (and so changing the alignment of their direction with that of the environmental flow) while travelling in the bent-back cloud head. The magnitudes (and timing) of this oscillation vary between runs, indicating a difference in the SJ paths in their early stages of development. In the runs with coarser resolution this oscillation is much weaker (025deg) or even absent (04deg and jet35). This result suggests a different origin of the airstreams in these runs, and a more zonal path during their evolution, inconsistent with the exit of the airstream from a hooked cloud head (not shown). The oscillation is followed by an acceleration that starts around 10–12 hours before the identification time and ends around identification time, to reach wind speeds of $\sim$35–40 m s^{-1}. Although the maximum wind speed varies between runs, the SJs show a remarkable similarity in this strong acceleration (except in run jet35) which can thus be considered as one of the main characteristics of SJ evolution, along with the associated descent. The largest increase in speed occurs in the same experiments as those with the greatest total descent, exceeding 30 m s^{-1} in the SJs in runs jet50 and jet55 compared to 25 m s^{-1} in the control run. Conversely, the experiments with coarser resolution and reduced jet strength display a weaker acceleration.

The occurrence of SI on the SJ airstreams is revealed by the evolution of PV along the trajectories (Fig. 9c). In the control run and in the runs with enhanced jet strength (particularly jet55) the 25$^{\mathrm{th}}$ percentile and median values get close to or even below zero (the condition for the onset of SI) during the final part of the ascent and the beginning of the descent, in a time window centred around 10 hours before identification time. This suggests the occurrence and the subsequent release of SI in the SJ in these runs. Conversely, for the runs with coarser resolution and with reduced jet strength, PV values stay well above zero (particularly in run jet40) indicating the absence of substantial SI along the trajectories. The airstream in run jet35 displays an almost-constant PV throughout all its evolution, indicating the absence of non-negligible diabatic processes throughout its evolution. This, along with the low moisture content of the airstream (not shown) and the absence of a substantial acceleration and a strong descent towards low levels, indicates that this airstream is simply adiabatically advected and weakly accelerated above the boundary layer towards the frontal-fracture region. Hence, it does not fulfil the SJ criteria according to the definition in CG18; instead it might be part of — or associated with — the intrusion of dry air from upper levels.

A similar ocurrence of instability, but at an earlier time, exists for CSI, with 25$^{\mathrm{th}}$ percentile and even median values of MPV* in the control, jet50 and jet55 runs below zero at around 20 hours before identification time i.e. at the start of the coherent SJ airstream ascent into the cloud head (Fig. 9d). These median values then stay close to zero throughout the time when SI develops. Again, in the other runs these values are well above zero. The drop in MPV* in the jet55 run during the final hours of SJ descent can be ignored as that airstream is far from saturated at that time and hence the conditions for CSI release do not hold. The occurrence of CI is also ruled out as values of moist static stability (not shown) stay well above zero during the whole evolution of the airstreams in all runs, going down to negative values only at the end of the descent for jet55 (when CI cannot be released as the air is unsaturated).

As stated earlier, the selected possible SJ airstreams are less distinct from each another in the other subset of sensitivity experiments (Fig. 10). Time series of pressure and wind speed along the trajectories (Figs. 10a and b, respectively) show for all runs a similar ascent-descent pattern associated with a strong speed increase following an early oscillation, also quantitatively akin to the evolution described for the first subset of experiments. Hence, the description of the SJ undergoing a coherent saturated ascent associated with condensation and precipitation followed by a nearly-adiabatic descent associated with strong acceleration can be extended to the whole set of sensitivity experiments performed, with the exception of jet35. For SI on the SJs in this experiment subset, the 25$^{\mathrm{th}}$ percentile value of PV decreases to or below zero in the time window between 15 and 5 hours before identification time (i.e during the final part of the ascent and the start of the descent) in all runs apart from rh70 and t299 (Fig. 10). Hence SI exists on at least a quarter of the SJ trajectories in five out of the seven runs in this subset. Considering CSI instead, Fig. 10d shows that for all the SJs the 25$^{\mathrm{th}}$ percentile (and for most of them also the median) decreases to negative values of MPV* at around 15–20 hours before identification time, even though it increases soon after in the t299 run. Hence, the occurrence of CSI along the SJ during its ascent is common in these sensitivity experiments.

In summary, the analysis of the evolution of selected physical quantities along the SJ trajectories in the different sensitivity experiments highlights a common behaviour: a saturated-ascent/adiabatic-descent pattern and strong increase in wind speed associated with the descent of the airstream. Additionally, the analysis reveals the existence of different environmental conditions for the occurrence of SI along the SJs during their evolution. In the first subset of experiments, simulations with different percentages of SI on the trajectories are associated with different values in the strength of descent and maximum wind speed. In the second subset of experiments, whilst the range in the percentage of SI on trajectories is still present, the values of wind speed and pressure are instead very similar for all SJs throughout their evolution. As a whole, this indicates that model resolution and jet strength can change the intensity of the SJ whereas other environmental changes (e.g to initial relative humidity or surface temperature), while influencing the dynamics of the SJ generated (as indicated by the variations in SI), do not seem to have a clear effect on its intensity both in terms of peak speed and descent. It is also revealed that lower-tropospheric wind maxima in the frontal-fracture region can occur from airstreams being zonally and adiabatically transported by a weakly descending and accelerating flow associated with the intrusion of dry air in the same frontal-fracture region (as occurs in run

https://doi.org/10.5194/wcd-2019-8
Preprint. Discussion started: 1 October 2019

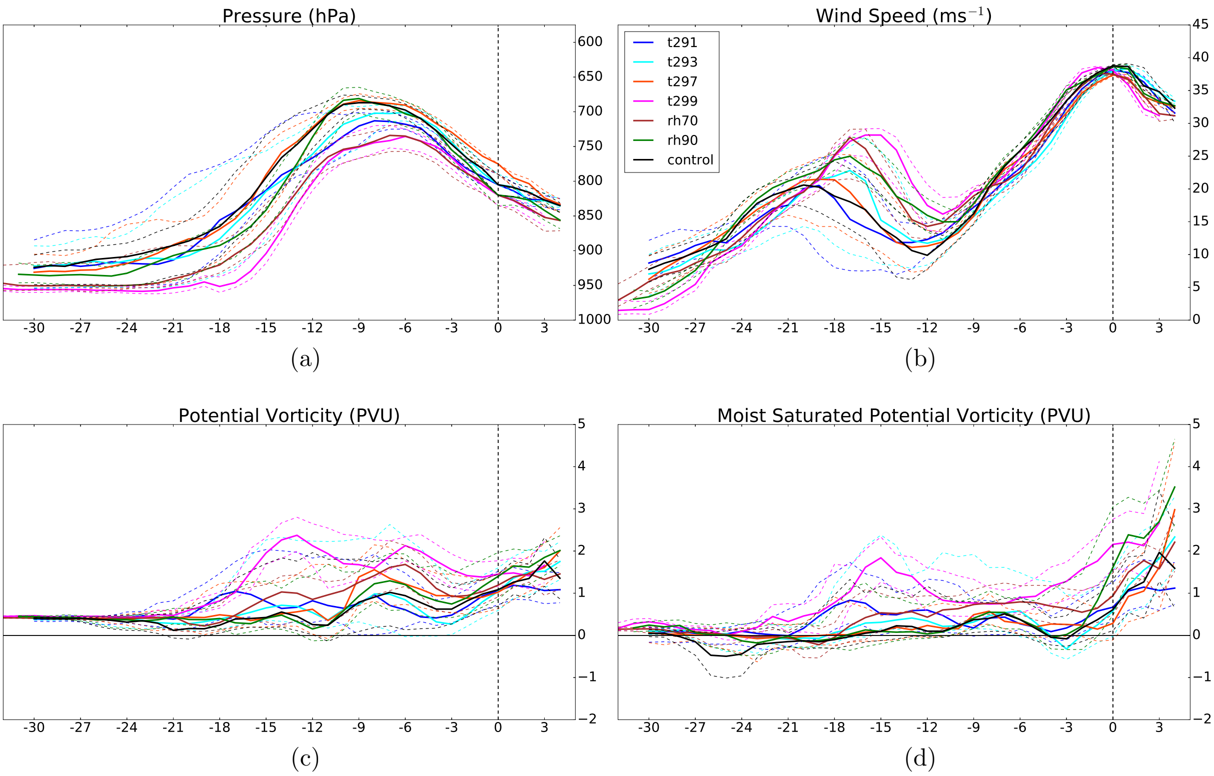

Figure 10. As in Fig. 9 but for the control simulation and for the runs with modified initial relative humidity (rh70, rh90) and initial temperature (t291, t293, t297, t299).

jet35). Hence, SJ identification requires the wind maxima to be associated with an airstream that exits from the cloud head and undergoes a descent associated with marked increase in wind speed.

3.2.3 Synthesis of the results

The control simulation has demonstrated that the SJ is closely associated with a band of negative or zero PV. As discussed in CG18, separating cause and effect is very difficult in that frontal circulations are known to have a strong impact on stability while even balanced dynamics is strongly modified as neutral stability is approached. Nevertheless, it is worthwhile considering what the sensitivity studies can tell us about the relationship between mesoscale instability and SJ properties, here expressed by wind speed and descent and summarised in the panels of Figure 11.

The mesoscale instability metrics used are essentially measures of SI. $trajs_{PV<0}$ is the maximum number of trajectories of the 100 selected with negative PV at any instant within 15 hours from the time when the trajectories are selected (i.e. identification time) and $volume_{PV<0}$ is the maximum percentage of SI-unstable volume in the cloud head around the SJ detected in the same time interval (see caption for more details). These metrics are compared in Fig. 11a and found to correlate reasonably well but with substantial variability between cases, so it is likely that there is a degree of arbitrariness in the choice of metric. The simulations where surface temperature has been changed the most display the largest deviations from this correlation. In the following we consider just $trajs_{PV<0}$. The wind speed and descent metrics used are: the maximum Earth-relative wind speed, $|\mathbf{U}|$; the system-relative wind speed at the time of $|\mathbf{U}|$, $|\mathbf{U}|_{sys}$; the maximum pressure increase over the five hours before the time of $|\mathbf{U}|$, Δp_{5h}; and the total pressure increase and speed increment during SJ descent $\Delta p_{descent}$ and $\Delta|\mathbf{U}|_{descent}$, respectively.

Before considering the link between instability and SJ properties in all the simulations together, it is worth summarising results from each type of the experiments presented in the previous section. Most straightforward is the impact of horizontal resolution: lower resolution substantially reduces peak wind speed (both Earth-relative and system-relative, Figure 11b and c) and removes all SI. In the coarser resolution runs SI is absent with both $trajs_{PV<0}$ and $volume_{PV<0}$ equal to zero not only in the SJ but throughout the cloud head, as shown in Figure 11a. As discussed in Section 3.2.2, the impact of background jet strength is also very clear: higher jet strength leads to more unstable, stronger SJ winds (both Earth-relative and system-relative) and much more descent (Figure 11e). The three unstable cases have $|\mathbf{U}|$ 10 m s^{-1} stronger and $|\mathbf{U}|_{sys}$ 5 m s^{-1} stronger than the two stable ones with jet strength 40 m s^{-1} and below; in fact case jet35 has already been noted not to have SJ characteristics at all. The relationship is not linear or even monotonic, as "saturation" appears to happen for the strongest background jet with the SJ in the jet50 experiment having stronger $|\mathbf{U}|$ than that in the jet55 experiment. This reduction is accompanied by a qualitative change in cyclone structure (not shown). Changes in relative humidity have little effect on $|\mathbf{U}|$, but an approximately linear impact on Δp_{5h}. Notably, the instability marginally increases over the control in case rh90, but decreases much more in rh70. It seems likely that this reflects the non-linearity of the sub-grid cloud condensation scheme. Surface temperature also has relatively small detectable impact: $|\mathbf{U}|$ and instability ($trajs_{PV<0}$) decrease slightly at lower temperatures, but the highest temperature (t299) has the smallest instability (essentially stable) and yet the largest $|\mathbf{U}|$ and $|\mathbf{U}|_{sys}$ values.

When grouped together, the first thing to note is the existence of two subsets of cases: SJs termed here as being either unstable or stable to SI release as determined from $trajs_{PV<0}$ (Figure 11a). The six stable cases comprise two with zero values of $trajs_{PV<0}$ (those in the runs with with coarser resolution than the control run) and four with $0 < trajs_{PV<0} \leq 10$ (those in the runs with reduced jet strength, including non-SJ case jet35, and cases t299 and rh70). In contrast, the seven unstable cases all have $trajs_{PV<0} \geq 25$.

Discounting the non-SJ jet35 case, the $|\mathbf{U}|$ values reached by different SJ airstreams are generally within 37 and 40 m s $^{-1}$ despite the range of environmental conditions (Fig. 11b). It is particularly notable that simply increasing the background jet strength does not provide much scope for increase in SJ strength as it eventually leads to a change in cyclone structure. We have yet to find an idealised background state able to produce the more extreme SJs such as the Great Storm of 1987 and cyclone Tini. On average, unstable SJs have larger $|\mathbf{U}|$ values, with a weak tendency for this windspeed to increase with instability. The emerging picture displays SJ strengths in the mid 30s m s^{-1} in stable cases being enhanced by around 5 m s^{-1} although the variability between experiments reduces the clarity of this effect. However, much of this signal comes from the jet strength and resolution experiments; the remaining two of the stable SJs and four of the unstable ones have very similar $|\mathbf{U}|$ with values

https://doi.org/10.5194/wcd-2019-8
Preprint. Discussion started: 1 October 2019

between 37 and 39 $\mathrm{m\,s^{-1}}$. We assume that one effect of changing the RH is to change the effective static stability and hence available potential energy of the background state; however, as cloud formation occurs it is difficult to quantify the magnitude of this. On the other hand, the behaviour of the t299 case is a real outlier.

In Sec. 3.1.3 we showed that, during their descent, SJ trajectories in the control simulation increased their system-relative speed by around 5 $\mathrm{m\,s^{-1}}$. The uncertainty in system speed discussed in Sec. 2.5 means that it is difficult to measure changes in system-relative speed of this magnitude. The relationship between system-relative speed and SI is displayed in Figure 11c. The impact of resolution and background jet strength is, perhaps, clearer than in Figure 11b, but cases rh70 and t299 show even more similarity in terms of $|\mathbf{U}|_{sys}$ to high instability cases. Overall, it is difficult to assert a strong relationship between either Earth-relative or system-relative SJ maximum speed and degree of SI. Some relationship between instability and amount of descent is instead evident in Figure 11d; this would be further strengthened if the resolution experiments were ignored, as clearly resolution changes the overall behaviour of the cyclone in ways different from just changing the background state.

A strong correlation between descent and speed increment can be expected from dynamical arguments as the descent is largely radial with respect to the cyclone centre; the speed increment can then be associated with the work done by the horizontal pressure gradient on the ageostrophic motion. However, the ageostrophic acceleration by the horizontal pressure gradient is the only source of horizontal kinetic energy (friction is a sink) whether the flow is balanced or not so this tells us nothing about mechanism. This correlation is investigated in Fig. 11e, comparing the total descent and the associated speed increment of SJs moving from the cloud head towards the frontal-fracture region. Neglecting the zonally-moving non-SJ jet35 case, a somewhat linear relationship is present overall, though still with substantial noise and no pattern in the surface temperature experiments when taken alone. The anomalously low value of $\Delta|\mathbf{U}|_{descent}$ for jet55 is a consequence of a late start of the SJ descent, possibly associated with a different cloud-head structure, meaning that some of the speed increment of the SJ trajectories is not considered. A clearer relationship is instead visible between Δp_{5h} and $|\mathbf{U}|$ (the magnitude of steepest descent and the peak Earth-relative speed) (Fig. 11f), although this comparison is less dynamically meaningful than the previous one.

We have not attempted to refine these relationships using more objective statistical tests, as we do not feel the heterogenous nature of the data set justifies doing so. There seems to be overall some evidence that weakly enhanced SJ strength is *associated* with increased SI, but clearly other processes are occurring in the different cases to complicate behaviour.

https://doi.org/10.5194/wcd-2019-8
Preprint. Discussion started: 1 October 2019

Weather and Climate Dynamics Discussions
Open Access
EGU

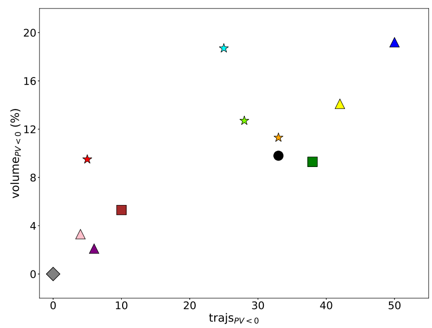

(a)

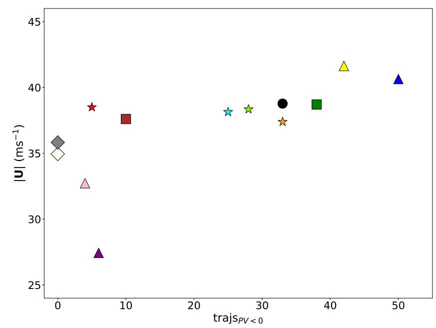

(b)

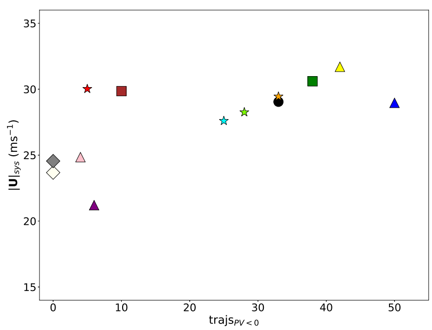

(c)

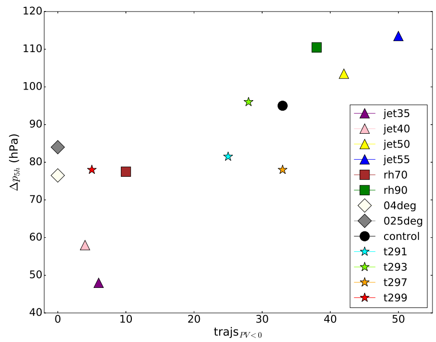

(d)

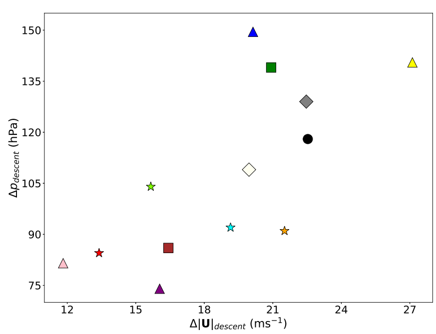

(e)

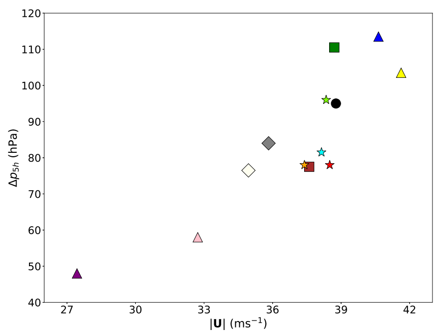

(f)

Figure 11. Scatterplots showing, for all the sensitivity experiments: (a) volume$_{PV<0}$ against $trajs_{PV<0}$, (b) $|\mathbf{U}|$ against $trajs_{PV<0}$, (c) $|\mathbf{U}|_{sys}$ against $trajs_{PV<0}$, (d) Δp_{5h} against $|\mathbf{U}|$, (e) Δp_{5h} against $trajs_{PV<0}$ and (f) $\Delta|\mathbf{U}|$ against $trajs_{PV<0}$. $trajs_{PV<0}$ is the maximum number of trajectories of the 100 selected with negative PV at any instant within 15 hours from the time when the trajectories are selected (i.e. identification time) and $volume_{PV<0}$ indicates the maximum percentage of grid points with negative PV, evaluated in the same time window as $trajs_{PV<0}$, in a volume centred on the location of the median of trajectories and extending for 20 grid points in latitude, 40 grid points in longitude and 3 vertical pressure levels. $|\mathbf{U}|$ is the maximum Earth-relative speed, $|\mathbf{U}|_{sys}$ is the system-relative speed at the time when $|\mathbf{U}|$ is reached, Δp_{5h} is the maximum pressure increase in five hours, and $\Delta p_{descent}$ and $\Delta|\mathbf{U}|_{descent}$ indicate, respectively, total pressure increase and speed increment during descent. The end of the descent is taken at identification time and its start has to be not more than twelve hours before. All these kinematic quantities refer to the median of trajectories.

https://doi.org/10.5194/wcd-2019-8
Preprint. Discussion started: 1 October 2019

3.2.4 Comparison with previous studies

A comparison of these results with previous idealised case studies reveals that the typical values of peak wind speed (37-40 $\mathrm{m\,s^{-1}}$) are close to those in the high-high resolution simulation in Coronel et al. (2016) (whose SJ trajectories peak at 40-43 $\mathrm{m\,s^{-1}}$) and more than 10 $\mathrm{m\,s^{-1}}$ higher than in the control simulation in Baker et al. (2014). As the Baker et al. (2014) values are substantially lower than in observed events and simulated SJ case studies (listed in CG18), this is a further proof of the benefits of the improved initial balanced state in producing idealised extratropical cyclones containing a realistic SJ. The maximum values of 5-hour descent (typically around 80–110 hPa in the simulations presented in this study) are instead similar to those in both of these previously-published idealised simulations. Sensitivity runs in Baker et al. (2014) highlight that a reduction in tropospheric static stability substantially increases the strength of descent and acceleration of the SJ, and vice versa. This static stability reduction is associated with a marked decrease in inertial stability and thus indicates a possible role of dry mesoscale instabilities in SJ strengthening. This role is also highlighted here using a more extensive set of simulations, as is the general increase in SJ maximum wind speed and descent rate with increasing upper-level jet strength diagnosed in the additional experiments in Baker (2011).

Coronel et al. (2016) use sensitivity experiments to horizontal and vertical model grid spacing to highlight the model resolution constraints for correct simulation (and in some cases even generation) of SJs in numerical simulations. Our findings are also in agreement with theirs in that our coarser resolution simulations contain the weakest SJs with no sign of SI in their cloud-head environments. Coronel et al. (2016) found regions near-neutral to CSI close to the bent-back slanted frontal zone and revealed the possible occurrence of II in the same area. The work presented here confirms this finding by showing the presence of regions of negative PV and clarifies its generation mechanism, which is found to be consistent with the conceptual model detailed in Volonté et al. (2018). Therefore, while Coronel et al. (2016) emphasise dynamical geostrophic forcing as the main mechanism driving SJ evolution, our work reveals the generation of symmetrically unstable areas in the cloud head and along the SJ, the release of which strengthens the SJ and ultimately shapes its evolution.

In summary, the relevant findings from previous idealised works are consistent with the results presented here. As a consequence of using realistic environmental states and a wide and different set of sensitivity experiments, this study also constitutes a step forward in SJ research as it highlights the role of dry mesoscale instabilities in SJ evolution, clarifying the underlying dynamics while showing the robustness of SJ occurrence in intense Shapiro-Keyser extratropical cyclones.

4 Conclusions

Idealised simulations of Shapiro-Keyser cyclones developing a SJ are presented in this study. The setup and initial state of the simulations follow from Baker et al. (2014) which is in turn based on the LC1 baroclinic lifecycle in Thorncroft et al. (1993) (with the addition of moisture). Thanks to an improved and accurate implementation of thermal wind balance in the initial state, it has been possible to use a realistic temperature profile without suffering from the static stability issues that occurred in the Baker et al. (2014) study.

The control simulation produces a cyclone that fits the Shapiro-Keyser conceptual model and develops a SJ (control SJ hereafter) whose dynamics are associated with the evolution of symmetric instability along the airstream. The control SJ shows values of wind speed and descent comparable with previous case studies, including the idealised simulations in Coronel et al. (2016), although smaller than in the simulation of windstorm Tini (Volonté et al., 2018). The control SJ is an airstream that develops from air ascending up to 700 hPa into the cloud head before undergoing a descent of around 95 hPa in five hours while leaving the cloud-head banded tip and travelling towards the frontal-fracture region (a region of buckling of the already-sloped θ_w lines). While flowing into this region, the SJ accelerates strongly to produce a peak wind speed close to 40 $\mathrm{m\,s^{-1}}$. The control SJ also increases its speed in a system-relative framework, although to a lesser extent than the SJ in the simulation of windstorm Tini. This acceleration suggests a link with mesoscale processes on top of the synoptic evolution. The occurrence of condensation during the ascent of the airstream is evident while evaporative/sublimational cooling at the start of the descent is much less so.

The analysis of the evolution of mesoscale instabilities along the control SJ shows that, in addition to CSI, both SI and II are present in more than 30% of the trajectories just before the start of the SJ's descent, after which the proportion of unstable trajectories gradually decreases towards zero. This evolution indicates the possible role of dry mesoscale instabilities (such as SI and II) in the dynamics of SJ acceleration and descent, although the maximum number of trajectories unstable to dry mesoscale instabilities is substantially fewer than in windstorm Tini. While Coronel et al. (2016) also reveal the possible occurrence of dry instabilities in the area of the bent-back front, here we were able to assess the underlying mechanism. Negative PV (condition for SI) is generated along the narrow and slanted frontal zone in the cloud head and then travels with the airstream towards the frontal fracture before being released during the SJ descent. The evolution of SI thus follows the conceptual model outlined in Volonté et al. (2018).

Sensitivity experiments have been performed by varying model resolution and initial values of upper-tropospheric jet strength, sea surface temperature and relative humidity. All of the 13 simulations display a Shapiro-Keyser cyclone that evolves similarly to the control simulation and show a low-level wind maximum in the frontal-fracture region. In the simulation with the weakest jet stream this wind maximum is associated with a zonally and adiabatically transported airstream possibly associated with dry-air intrusion. In all other 12 simulations the frontal-fracture wind maxima are instead associated with SJs, i.e. airstream exiting from the cloud head and undergoing a descent while markedly increasing their wind speed (see definition in CG18). These experiments thus display the SJ as a robust feature of intense Shapiro-Keyser cyclones, across a wide range of environmental conditions.

Selected physical quantities along the SJ trajectories have been analysed in the different sensitivity experiments revealing a common SJ behaviour: a saturated-ascent/adiabatic-descent pattern and strong increase in wind speed (up to 37–40 $\mathrm{m\,s^{-1}}$) associated with the descent (80–110 hPa/5h) of the airstream. This analysis also shows a range of different environmental conditions leading to the occurrence of SI along the SJs during their evolution. Whilst variations to model resolution and jet strength can change the intensity of the SJ, other environmental changes (e.g to initial moisture or temperature) do not seem to have a clear effect on its intensity both in terms of peak speed and descent while still influencing the dynamics of the SJ generated (as indicated by the variations in SI). Synthesis diagrams aimed at assessing the existence of a relationship between

https://doi.org/10.5194/wcd-2019-8
Preprint. Discussion started: 1 October 2019

dynamical drivers and kinematic effects of the SJ evolution in the different simulations demonstrate the existence of two subsets of airstreams: six 'stable SJs' and seven 'unstable SJs' based on the number of trajectories unstable to SI during their evolution. On average, unstable SJs show slightly faster wind speeds and larger descents although substantial noise is present.

In summary, this study uses idealised simulations to explore the evolution of SJs in extratropical cyclones and assess the robustness of their occurrence and dynamics with respect to different environmental conditions. Thanks to an improved initial balance, it has been possible to use more realistic environments than in previous idealised studies (Baker et al., 2014; Coronel et al., 2016). While confirming the relevant findings from previous idealised studies, the choice of a wide and a different range of sensitivity experiments allows further insight into the analysis of SJ evolution and dynamics in different environmental conditions. The conceptual model of SJ generation and strengthening outlined in Volonté et al. (2018) is reproduced by the control simulation, which shows a clear contribution of SI generated by slantwise frontal motions in the cloud head in the evolution of the SJ. The sensitivity experiments reveal the SJ as a robust feature of intense Shapiro-Keyser cyclones, highlighting a range of different environmental conditions (conditional on the model having adequate resolution) in which the release of SI and other mesoscale instabilities contribute to the evolution of this airstream. The airstream's strength is overall weakly enhanced in SJs with increased SI, both in terms of speed and descent. However, several environmental factors modulate this relationship, making it difficult to disentangle the net effect of instability release. While further dedicated studies are needed to fully quantify the effect of dry instabilities in SJ dynamics, this idealised work confirms and clarifies their role in the evolution of the SJ, here shown as a robust feature of intense Shapiro-Keyser extratropical cyclones.

Code availability. The source code for the MetUM is available to use. To apply for a license for the MetUM go to:
https://www.metoffice.gov.uk/research/approach/collaboration/unified-model/partnership.
For more information on the exact model versions and branches applied please contact the authors

Data availability. Output data from the model simulations are currently stored in a local archive. Their transfer to an externally-accessible location is in the process of being discussed.

Author contributions. AV performed the simulations and the data analysis while thoroughly discussing experimental design and results with PC and SG. PC developed the idealised model and prepared its description for the manuscript. SG's contribution was essential in improving the first version of the manuscript, prepared by AV and reviewed by both PC and SG.

Competing interests. The authors declare that they have no conflict of interest.

https://doi.org/10.5194/wcd-2019-8
Preprint. Discussion started: 1 October 2019

Acknowledgements. The authors wish to thank the Met Office for making the MetUM available and the National Centre for Atmospheric Science Computational Modelling Services for supporting the academic use of the MetUM on the UK National Supercomputing Service, ARCHER. This work was supported by the AXA Research Fund project "Sting Jet Windstorms in Current and Future Climates." The authors would also like to thank Michael Sprenger (IAC-ETHZ) for his continuous support with the Lagranto code.

https://doi.org/10.5194/wcd-2019-8
Preprint. Discussion started: 1 October 2019

References

Arakawa, A. and Lamb, V. R.: Computational design of the basic dynamical processes of the UCLA general circulation model., Methods Comput. Phys., 17, 173–265, 1977.

Baker, L. H.: Sting jets in extratropical cyclones, Ph.D. thesis, University of Reading, 2011.

Baker, L. H., Gray, S. L., and Clark, P. A.: Idealised simulations of sting-jet cyclones, Q. J. R. Meteorol. Soc., 140, 96–110, https://doi.org/10.1002/qj.2131, 2014.

Bennetts, D. A. and Hoskins, B. J.: Conditional symmetric instability - a possible explanation for frontal rainbands, Q. J. R. Meteorol. Soc., 105, 945–962, 1979.

Boutle, I., Belcher, S., and Plant, R.: Moisture transport in midlatitude cyclones, Q. J. R. Meteorol. Soc., 137, 360–373, 2011.

Browning, K. A.: The sting at the end of the tail: Damaging winds associated with extratropical cyclones, Q. J. R. Meteorol. Soc., 130, 375–399, 2004.

Browning, K. A., Smart, D. J., Clark, M. R., and Illingworth, A. J.: The role of evaporating showers in the transfer of sting-jet momentum surface, Q. J. R. Meteorol. Soc., 141, 2956–2971, doi: 10.1002/qj.2581, 2015.

Büeler, D. and Pfahl, S.: Potential Vorticity Diagnostics to Quantify Effects of Latent Heating in Extratropical Cyclones. Part I: Methodology, J. Atmos. Sci., 74, 3567–3590, https://doi.org/10.1175/JAS-D-17-0041.1, 2017.

Charney, J. G. and Phillips, N. A.: Numerical integration of the quasi-geostrophic equations for barotropic and simple baroclinic flows, J. Meteor., 10, 71–99, 1953.

Clark, P. A. and Gray, S. L.: Sting jets in extratropical cyclones: a review, Q. J. R. Meteorol. Soc., 144, 943–969, https://doi.org/10.1002/qj.3267, https://rmets.onlinelibrary.wiley.com/doi/abs/10.1002/qj.3267, 2018.

Clark, P. A., Browning, K. A., and Wang, C.: The sting at the end of the tail: Model diagnostics of fine-scale three-dimensional structure of the cloud head, Q. J. R. Meteorol. Soc., 131, 2263–2292, 2005.

Coronel, B., Ricard, D., Rivière, G., and Arbogast, P.: Cold-conveyor-belt jet, sting jet and slantwise circulations in idealized simulations of extratropical cyclones, Q. J. R. Meteorol. Soc., 142, 1781–1796, 2016.

Davies, T., Cullen, M. J. P., Malcolm, A. J., Mawson, M. H., Staniforth, A., White, A. A., and Wood, N.: A new dynamical core for the Met Office's global and regional modelling of the atmosphere, Q. J. R. Meteorol. Soc., 131, 1759–1782, doi:10.1256/qj.04.101, 2005.

Durran, D. R. and Klemp, J. B.: On the Effects of Moisture on the Brunt-Väisälä Frequency, J. Atmos. Sci., 39, 2152–2158, 1982.

Edwards, J. and Slingo, A.: Studies with a flexible new radiation code. Part I: Choosing a configuration for a large-scale model, Q. J. R. Meteorol. Soc., 122, 689–719, doi:10.1002/qj.49712253107, 1996.

Grams, C. M. and Archambault, H. M.: The Key Role of Diabatic Outflow in Amplifying the Midlatitude Flow: A Representative Case Study of Weather Systems Surrounding Western North Pacific Extratropical Transition, Monthly Weather Review, 144, 3847–3869, https://doi.org/10.1175/MWR-D-15-0419.1, https://doi.org/10.1175/MWR-D-15-0419.1, 2016.

Gregory, D. and Rowntree, P. R.: A mass flux convection scheme with representation of cloud ensemble characteristics and stability-dependent closure, Mon. Weather Rev., 118, 1483–1506, 1990.

Hart, N. C. G., Gray, S. L., and Clark, P. A.: Sting-Jet Windstorms over the North Atlantic: Climatology and Contribution to Extreme Wind Risk, J. Climate, 30, 5455–5471, https://doi.org/10.1175/JCLI-D-16-0791.1, 2017.

Lock, A. P., Brown, A. R., Bush, M. R., Martin, G. M., and Smith, R. N. B.: A new boundary layer mixing scheme. Part I: Scheme description and single-column model tests, Mon. Weather Rev., 128, 3187–3199, 2000.

https://doi.org/10.5194/wcd-2019-8
Preprint. Discussion started: 1 October 2019

Martínez-Alvarado, O., Baker, L. H., Gray, S. L., Methven, J., and Plant, R. S.: Distinguishing the cold conveyor belt and sting jet air streams in an intense extratropical cyclone, Mon. Weather Rev., 142, 2571–2595, doi:10.1175/MWR-D-13-00348.1, 2014.

Martínez-Alvarado, O., Gray, S., Hart, N., Clark, P., Hodges, K., and Roberts, M.: Increased wind risk from sting-jet windstorms with climate change, Environ. Res. Lett., 13, 044 002, https://doi.org/10.1088/1748-9326/aaae3a, 2018.

Panagi, P.: NDdiag: A Fortran90 program to compute diagnostics on pressure levels from Unified Model data on model levels, accessed from https://puma.nerc.ac.uk/trac/UM_TOOLS/wiki/NDdiag, 2011.

Polvani, L. M. and Esler, J. G.: Transport and mixing of chemical air masses in idealized baroclinic lifecycles, J. Geophys. Res., 112, doi:10.1029/2007JD008555, 2007.

Shapiro, M. A. and Keyser, D.: Fronts, jet streams and the tropopause, in: Extratropical cyclones: the Erik Palmén memorial volume, edited by Newton, C. and E O Holopainen, E., pp. 167–191, American Meteorological Society, 1990.

Smart, D. J. and Browning, K. A.: Attribution of strong winds to a cold conveyor belt and sting jet, Q. J. R. Meteorol. Soc., 140, 595–610, https://doi.org/10.1002/qj.2162, 2014.

Smith, R. N. B.: A scheme for predicting layer clouds and their water content in a general circulation model, Q. J. R. Meteorol. Soc., 116, 435–460, https://doi.org/10.1002/qj.49711649210, 1990.

Sprenger, M. and Wernli, H.: The LAGRANTO Lagrangian analysis tool – version 2.0, Geosci. Model Dev., 8, 2569–2586, https://doi.org/10.5194/gmd-8-2569-2015, 2015.

Thorncroft, C. D., Hoskins, B. J., and McIntyre, M. E.: Two paradigms of baroclinic-wave life-cycle behaviour, Q. J. R. Meteorol. Soc., 119, 17–56, 1993.

Volonté, A.: Dynamics of sting jets and their relation to larger-scale drivers, Ph.D. thesis, University of Reading, 2018.

Volonté, A., Clark, P. A., and Gray, S. L.: The Role of Mesoscale Instabilities in the Sting-Jet dynamics of Windstorm Tini, Q. J. R. Meteorol. Soc., doi:10.1002/qj.3264, 2018.

Wernli, H. and Davies, H. C.: A Lagrangian-based analysis of extratropical cyclones. I: The method and some applications, Q. J. R. Meteorol. Soc., 123, 467–489, 1997.

White, A. A., Hoskins, B. J., Roulstone, I., and Staniforth, A.: Consistent approximate models of the global atmosphere: shallow, deep, hydrostatic, quasi-hydrostatic and non-hydrostatic, Q. J. R. Meteorol. Soc., 131, 2081–2107, https://doi.org/10.1256/qj.04.49, https://rmets.onlinelibrary.wiley.com/doi/abs/10.1256/qj.04.49, 2005.

Wilson, D. R. and Ballard, S. P.: A microphysically based precipitation scheme for the UK Meteorological Office Unified Model, Q. J. R. Meteorol. Soc., 125, 1607–1636, 1999.

Wood, N., Staniforth, A., White, A., Allen, T., Diamantakis, M., Gross, M., Melvin, T., Smith, C., Vosper, S., Zerroukat, M., and Thuburn, J.: An inherently mass-conserving semi-implicit semi-Lagrangian discretization of the deep-atmosphere global non-hydrostatic equations, Q. J. R. Meteorol. Soc., 140, 1505–1520, 2014.